AGU PUBLICATIONS

JGR

Journal of Geophysical Research: Oceans

RESEARCH ARTICLE

10.1002/2015JC011265

Sea level anomaly on the Patagonian continental shelf: Trends, annual patterns and geostrophic flows

L. A. Ruiz Etcheverry[1,2,3,4], M. Saraceno[1,2,3], A. R. Piola[1,3,5], and P. T. Strub[6]

[1]Departamento de Ciencias de la Atmósfera y los Océanos, Universidad de Buenos Aires, Buenos Aires, Argentina, [2]Centro de Investigación del Mar y la Atmósfera, Buenos Aires, Argentina, [3]Instituto Franco Argentino para el estudio del clima y sus impactos (UMI-IFAECI), Argentina, [4]Now at International Pacific Research Center School of Ocean and Earth Science and Technology, University of Hawaii at Manoa, Honolulu, Hawaii, [5]Departamento Oceanografía, Servicio de Hidrografía Naval, Buenos Aires, Argentina, [6]College of Earth, Ocean and Atmospheric Sciences, Oregon State University, Corvallis, Oregon, USA

Abstract We study the annual patterns and linear trend of satellite sea level anomaly (SLA) over the southwest South Atlantic continental shelf (SWACS) between 54°S and 36°S. Results show that south of 42°S the thermal steric effect explains nearly 100% of the annual amplitude of the SLA, while north of 42°S it explains less than 60%. This difference is due to the halosteric contribution. The annual wind variability plays a minor role over the whole continental shelf. The temporal linear trend in SLA ranges between 1 and 5 mm/yr (95% confidence level). The largest linear trends are found north of 39°S, at 42°S and at 50°S. We propose that in the northern region the large positive linear trends are associated with local changes in the density field caused by advective effects in response to a southward displacement of the South Atlantic High. The causes of the relative large SLA trends in two southern coastal regions are discussed as a function meridional wind stress and river discharge. Finally, we combined the annual cycle of SLA with the mean dynamic topography to estimate the absolute geostrophic velocities. This approach provides the first comprehensive description of the seasonal component of SWACS circulation based on satellite observations. The general circulation of the SWACS is northeastward with stronger/weaker geostrophic currents in austral summer/winter. At all latitudes, geostrophic velocities are larger (up to 20 cm/s) close to the shelf-break and decrease toward the coast. This spatio-temporal pattern is more intense north of 45°S.

Key Points:
- Trends, annual patterns, and currents are analyzed with altimetry data
- Annual changes in sea level over the Patagonian shelf are mostly due to steric effects
- The general circulation in the region is northeastward with seasonal variability

Correspondence to:
L. A. Ruiz Etcheverry,
lruiz@cima.fcen.uba.ar

Citation:
Ruiz Etcheverry, L. A., M. Saraceno, A. R. Piola, and P. T. Strub (2016), Sea level anomaly on the Patagonian continental shelf: Trends, annual patterns and geostrophic flows, *J. Geophys. Res. Oceans*, *121*, 2733–2754, doi:10.1002/2015JC011265.

Received 24 AUG 2015
Accepted 21 MAR 2016
Accepted article online 24 MAR 2016
Published online 22 APR 2016

The copyright line for this article was changed on 12 AUG 2016 after original online publication.

© 2016. The Authors.
This is an open access article under the terms of the Creative Commons Attribution-NonCommercial-NoDerivs License, which permits use and distribution in any medium, provided the original work is properly cited, the use is non-commercial and no modifications or adaptations are made.

1. Introduction

1.1. Southwestern Atlantic Shelf Circulation

The Argentine Continental Shelf is part of the Southwestern Atlantic Continental Shelf (SWACS), which is the largest continental shelf of the southern hemisphere. The shelf width ranges between ∼170 and ∼850 km considering the 200 meter isobath as the eastern margin of the shelf, where a pronounced shelf-break clearly sets the boundary between the continental shelf and open ocean waters. Along the shelf-break the Malvinas Current (MC) flows northward, carrying cold waters from the Antarctic Circumpolar Current (Figure 1). At approximately 38°S the MC collides with the southward Brazil Current (BC), which carries subtropical warm and salty waters.

Numerical models indicate that the general circulation of the shelf consists of a northeastward flow between 55°S and 33°S (Figure 1). Close to the coast the morphology of the coastline affects the circulation, creating gyres and recirculations within several large-scale gulfs [*Palma et al.*, 2004a]. Over the shelf, coastal waters are separated from midshelf waters by a tidal front which marks the transition from vertically homogeneous coastal waters to well stratified waters occupying the mid and outer shelf from late spring to early fall [*Bianchi et al.*, 2005].

Strong tides [*Glorioso and Flather*, 1997; *Palma et al.*, 2004a], large freshwater discharges [*Piola et al.*, 2005], highly variable winds [*Palma et al.*, 2004b, 2008], and the influence of the MC along the continental shelf-break [*Palma et al.*, 2008; *Matano et al.*, 2010] are important contributors to the large-scale shelf circulation.

Due to the scarcity of observations the majority of the studies of the SWACS circulation are based on numerical models. Despite their value, in-situ observations are spatially and temporally inhomogeneous in

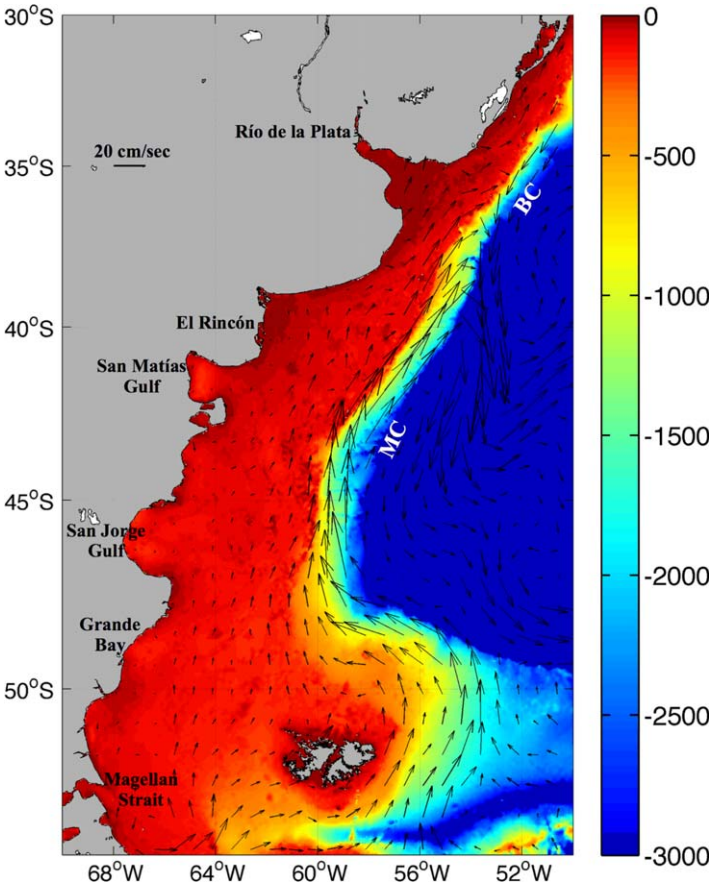

Figure 1. Mean circulation in the Southwestern Atlantic region derived from mean dynamic topography. Bottom topography (in meters), from version 8.2 [*Smith and Sandwell*, 1997]. MC: Malvinas Current, BC: Brasil Current.

the region. In contrast, satellites provide homogeneous spatially and temporally distributed data. In particular, satellite altimetry provides more than 20 years of Sea Level Anomaly (SLA) and is therefore a useful tool to study the circulation.

1.2. Satellite Altimetry

Since the launch of the TOPEX/POSEIDON missions in October 1992, satellite altimetry has greatly contributed to our understanding of the general circulation of the ocean. Recent improvements in the correction terms used to compute satellite SLA have encouraged the extension of circulation studies closer to the coast and over continental shelves. For example, gridded maps of SLA derived from Archiving, Validation and Interpretation of Satellite Oceanographic (AVISO) have been shown to adequately represent the annual cycle of sea level over most continental shelves and coastal areas [*Ruiz Etcheverry et al.*, 2015]. Similar results were found based on the analysis of TOPEX/POSEIDON along-track SLA data [*Vinogradov and Ponte*, 2010]. Both above-cited studies agree that there are some regions where a poor performance of the altimeter is due to local phenomena. At regional scales, altimetry data were successfully used to characterize the seasonal variability in regions such as Gulf of Cadiz [*Gomez-Enri et al.*, 2012; *Laiz et al.*, 2013], Nordic Seas [*Volkov and Pujol*, 2012], Baltic Sea [*Passaro et al.*, 2015] and the Río de la Plata (RdP) estuary [*Saraceno et al.*, 2014; *Strub et al.*, 2015], among others. In particular, in the RdP estuary (Figure 1), that is part of the SWACS, the observed pattern of seasonal SLA variations is due to a combination of solar radiation and wind forcing [*Saraceno et al.*, 2014]. The seasonal wind-forced and interannual SLA pattern documented using satellite altimetry by *Saraceno et al.* [2014] is in agreement with those observed in previous studies using a variety of data and numerical simulations [e.g., *Simionato et al.*, 2007; *Piola et al.*, 2005; *Palma et al.*, 2008].

1.3. Seasonal SLA

Rising and lowering of seasonal sea level is the result of the combination of the barometric component, steric effect (or buoyancy fluxes), mesoscale circulation and the contribution of the bottom pressure [*Gill and Niiler*, 1973]. Hydrological (river runoff) forcing can also affect the sea level variability at regional scales [*Tsimplis and Woodworth*, 1994]. The barometric component is eliminated from the altimetry data and the bottom pressure is associated with changes in the wind stress [*Gill and Niiler*, 1973; *Song and Qu*, 2011].

At large scales, it has been shown that in the open ocean the steric component of the seasonal SLA variations is dominated by the thermal effects while the salinity contribution plays a minor role and can be generally neglected [*Ferry and Reverdin*, 2000; *Stammer*, 1997; *Leuliette and Wahr*, 1999]. A counter example is in the North Atlantic, where the halosteric component contributes to the sea level, even though its effect is smaller than that of the thermosteric component [*Ivchenko et al.*, 2008].

The steric effect contributes significantly to the sea level trend. In particular, the thermosteric component in the upper 750 meters of the ocean is associated with global warming [*Lombard et al*. 2009; *Levitus et al*., 2012]. Altimetry data provide a means for continuous monitoring of temporal and spatial sea level variations, which are key factors to globally and locally monitor climate change effects [*Cazenave and Llovel*, 2010].

In general, the seasonal cycle of sea level in coastal areas is also dominated by the steric-effects [e.g., *Bell and Goring*, 1998; *Laiz et al*., 2013]. Another effect that can play an important role in the seasonal variability is the wind forcing. The region surrounding and north of the RdP estuary is an example of a region affected by the wind, as above [*Saraceno et al*., 2014; *Matano et al*., 2014; *Strub et al*., 2015]. The coast of Chile is another example where the seasonal SLA is mostly explained by changes in along-shore winds [*Aguirre et al*., 2012]. The annual signal of sea level can also be influenced by nearby river discharge. For example, *Tsimplis and Woodworth* [1994] observed large annual amplitude of SLA in the Bay of Bengal and Bohai Bay, which are partly attributed to large continental runoff.

1.4. Article Organization

In this article we document the seasonal (annual cycle) component of the altimetry SLA in the SWACS (36°S–54°S and 70°W–52°W) and investigate the possible causes of the spatial patterns of the observed amplitude and phase. We also analyze the linear trends of sea level and the geostrophic velocities associated with the annual cycle of absolute dynamic topography. The article is organized as follows: the data and methods are described in sections 2 and 3, respectively. Section 4 presents the results and discussion and section 5 summarizes the main conclusions.

2. Data

2.1. Satellite Altimetry

We used the merged gridded SLA daily maps produced by Ssalto/Duacs and distributed by AVISO (www.aviso.oceanobs.com) for the 21 year period January 1993 to December 2013. The delayed time all-sat (DT all-sat) product is used because it is more precise than near-real time data and has the best possible spatial and temporal sampling. The SLA product is computed with the Mean Sea Surface MSS CNES-CLS-2011 referenced to a 20 years period (1993–2012) [AVISO, 2014].

To generate the DT all-sat gridded data, all the available satellite missions are used (TOPEX/POSEIDON, Jason-1, Geosat Follow-on, Jason-2, Envisat, ERS-1, ERS-2, Cryosat-2, Saral/Altika) which provide up to 4 satellites at a time. An optimal interpolation with realistic correlation functions is applied to produce SLA maps of 1/4° resolution [*AVISO*, 2014; *Ducet et al*., 2000]. In some cases, the interpolation produces values located over land. To avoid this problem, we built a continental mask as the union between the AVISO gridded data continental mask and all pixels with positive bathymetry (version 8.2) [*Smith and Sandwell*, 1997].

We also used the 1/4° resolution MDT CNES-CLS13 product from AVISO, which is an estimate of the ocean Mean Dynamic Topography (MDT) for the period 1993–2012. This MDT product is based on 2 years of Gravity field and Ocean Circulation Explorer (GOCE) data, 7 years of Gravity Recovery and Climate Experiment (GRACE) data, and 20 years of altimetry and in situ data (hydrologic and drifters data).

2.2. Net Heat Flux

Monthly Net Heat Flux (NHF) data for the period January 1993 to December 2009 was provided by Objectively Analyzed air-sea Fluxes (OAflux, http://oaflux.whoi.edu/data.html). OAflux and the International Satellite Cloud Climatology Project (ISCCP) compute a 1 degree gridded NHF as

$$NHF = SW_{down} - LW_{up} - LH_{up} - SH_{up} \quad (1)$$

where SW_{down}, LW_{up}, LH_{up} and SH_{up} are the incoming short wave radiation, the net outgoing long wave radiation (radiation emitted by the ocean minus the radiation emitted by the atmosphere), outgoing latent heat and sensible heat fluxes through the surface of the ocean, respectively. LH and SH are calculated as a function of surface meteorological and oceanographic variables (wind speed, air humidity and sea surface temperature) based on the Coupled Ocean-Atmosphere Response Experiment (COARE 3.0) model [*Yu et al*., 2004a]. The SW_{down} and LW_{up} are provided by ISCCP.

In addition, we use the heat fluxes from the NCEP Climate Forecast System Reanalysis (CFSR) (rda.ucar.edu). The CFSR was designed and executed as a global, high resolution, coupled atmosphere-ocean-land surface-sea ice system to provide the best estimate of the state of these coupled domains over the period 1979–2009. The CFSR includes coupling of the atmosphere and ocean during the generation of the 6 h guess fields, an interactive sea-ice model, and assimilation of satellite radiances by a grid-point statistical interpolation scheme over the entire period. The global atmosphere resolution of CFSR is 38 km with 64 levels (from the surface to 0.26 hPa). The global ocean is 0.25° at the equator, extending to a global 0.5° resolution beyond the tropics, with 40 levels. These products are available at an hourly time resolution and 0.5° horizontal resolution, but for the analyses reported here we use the monthly mean product. To estimate the NHF from CFSR (NHF_{CFSR}) using equation (1), we used the downward SW radiation and the upward LW, LH and SH for the period January 1993 to December 2009.

2.3. Hydrographic Data

To estimate the thermal expansion and saline contraction coefficients we used climatological monthly sea temperature (T) and salinity (S) from the World Ocean Atlas 2009 (WOA09) [*Boyer et al*., 2009] (https://www.nodc.noaa.gov/OC5/WOA09/pr_woa09.html). We calculated the density and the mixed layer depth (MLD) using a potential density criterion. The MLD is estimated as the depth above which the potential density differs by less than 0.125 kg m^{-3} from the surface value based on monthly averaged profiles [*Monterey and Levitus*, 1997]. These time-varying T and S values are averaged over the MLD and are used to compute the thermal expansion coefficient (α) and saline contraction coefficient (β) with the Gibbs-SeaWater (GSW) Oceanographic Toolbox [*McDougall and Barker*, 2011] that considers the Thermodynamic Equation of seawater 2010 (TEOS-2010). This toolbox was also used to calculate density profiles at each grid point of WOA09. In addition, in situ vertical profiles of T, S and potential density data provided by the Argentine Naval Hydrographic Service (SHN) were used to calculate the thermal expansion coefficient at specific locations to evaluate the use of WOA09 data to calculate gridded values of α.

2.4. Wind

We used daily wind stress from QuikSCAT data for the period January 2000 to December 2008. This product has a spatial resolution of 0.5° and is obtained from www.ifremer.fr/cersat/. The SeaWind scatterometer on the QuikSCAT satellite is a specialized microwave radar from which near-surface wind speed and direction over the oceans are estimated. To estimate surface wind stress (τ) from the scatterometer wind vector, the following formula is used:

$$\tau = (\tau_x, \tau_y) = \rho_a C_D W(u, v) \tag{2}$$

where W is the scatterometer wind speed, and u and v are the zonal component (positive eastward) and meridional component (positive northward). The surface wind is assumed to be parallel to the stress vector (τ). ρ_a is the density of the surface air equal to 1.225 kg m^{-3} and C_D is the drag coefficient derived by *Smith* [1988].

2.5. SST

Sea surface temperature (SST) was obtained from weekly (8 day composite), 9 km, level 3 MODIS (Moderate Resolution Imaging Spectroradiometer) AQUA. We used Level 3 data for the period January 2003 to December 2013 from http://oceancolor.gsfc.nasa.gov. The MODIS sensor onboard the NASA Aqua platform recorded SST since May 2002. This SST product is derived from the thermal IR (11–12 μm) channels during night-time.

3. Methodology

3.1. Steric Height Anomaly

Changes in the density field due to the ocean's exchange of heat and freshwater with the atmosphere affect the sea level. As a result, there is a contraction or expansion of the water column, denominated by the "steric effect" (η_s) [*Gill and Niiler*, 1973]. The steric variability of the sea level is to first order caused by the change of the heat content in the ocean on seasonal time scales, with the effects of freshwater exchange (salinity) playing a secondary role over most of the ocean [*Gill and Niiler*, 1973]. The steric sea level anomaly can be computed as follows:

$$\eta_s' = -\frac{1}{\rho_0}\int_{-H}^{0} \rho'(z)dz \tag{3}$$

where $\rho'(z,t) = \rho(z,t) - \bar{\rho}(z)$ is the time-dependent density anomaly relative to a reference profile [*Stammer*, 1997], ρ_0 is a reference water density, H is the water depth, but it can be also considered as the base of the seasonal thermocline since most of the seasonal steric changes occur above that level. In addition, equation (3) can be written as a function of temperature and salinity anomaly as follows:

$$\eta_s' = \left(\int_{-H}^{0} \alpha T' dz - \int_{-H}^{0} \beta S' dz\right) \tag{4}$$

where α and β are the thermal expansion and saline contraction coefficients, respectively. Since the thermal effect dominates the steric height variability [*Ferry and Reverdin*, 2000; *Stammer*, 1997; *Leuliette et al*., 1999], away from regions of large freshwater discharge and sharp salinity fronts, the second term of equation (4) can be neglected.

We then equate the net surface heat flux to the local change in heat storage as represented by the vertical temperature profile [*Stammer*, 1997] to estimate the rate of change in steric height anomaly due to surface heating alone:

$$\frac{\partial \eta_s'}{\partial t} = \frac{\propto NHF'}{\rho_0 c_p} \tag{5}$$

where *NHF′* represents the monthly anomalous net surface heat flux in the annual cycle, ρ_0 is a reference water density and $c_p \approx 4000$ J kg^{-1} K^{-1}, the specific heat of seawater. As stated in section 2.3, α is calculated with the GSW oceanographic toolbox. From equation (5) it is then possible to integrate in time to obtain the thermosteric height anomaly due to local surface heating.

3.2. Harmonic Analysis and Linear Trend

In the SWACS the seasonal cycle of SLA is well represented by the harmonic analysis of the gridded data produced by AVISO [*Ruiz Etcheverry et al*., 2015; *Saraceno et al*., 2014]. However, to corroborate this result we calculated the goodness of the fit (GoF) in the region. The GoF over most of the shelf region is higher than 80% (e.g., the annual harmonic explains more than 80% of the variance). Only south of Malvinas Islands and in the shelf-break between 40°S and 44°S the GoF is lower, probably due to recurrent intrusions of Malvinas Current waters onto the outer shelf [*Piola et al*., 2010]. In addition, following *Mork and Skagseth* [2005], we estimated the error of the amplitude and phase of the SLA annual cycle associated with the harmonic analysis. The error of the amplitude is lower than 1 cm representing less than 10% of the annual amplitude. In the annual phase, the errors also represent less than 10% of the values shown in Figure 3b, except near the shelf break (∼42°S) where the GoF has lower values. The results of the uncertainties introduced by the annual harmonic fit encouraged us to apply the same methodology to extract the annual signal from the SLA and SST data.

The harmonic analysis is an estimate of the time series represented by a sum of cosines with different amplitudes and phases:

$$y(t) = \bar{y} + \sum_{q=1}^{M} C_q \cos\left(2\pi f_q t - \theta_q\right) + y_r(t) \tag{6}$$

where C_q, f_q and θ_q are the constant amplitude, frequency and phase of the qth constituent, respectively, $\bar{y}$ is the record length mean value and y_r is the residual portion of the time series. The aim of the least-squares method is to minimize the squared difference between the original data and the fitted data.

For the computation of seasonal cycle of thermal steric height due to the surface heat flux anomaly (equation (5)), we extracted the annual cycle of α multiplied by *NHF′* using harmonic analysis. Thus, we can integrate equation (5) as follows:

$$\int d\eta = \frac{1}{\rho_0\ C_p}\int \alpha(t) NHF'(t) dt = \frac{1}{\rho_0\ C_p}\int y(t) dt \tag{7}$$

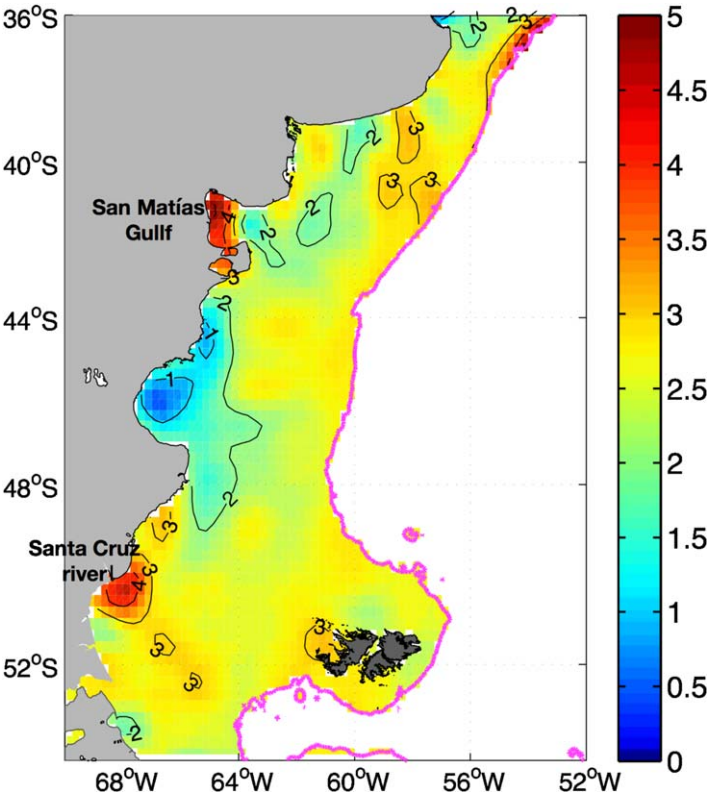

Figure 2. Distribution of linear trend of SLA (mm/yr) for the period January 1993 to December 2013. The magenta line indicates the 200 m isobath.

The thermal expansion coefficient derived from WOA is interpolated to the NHF grid before computing the thermal steric height.

Previous to the computation of the annual harmonic, we removed the linear trend from the SLA data. This trend is computed using a least square method and is tested with the Student-t test at the 95% confidence level (CL). Then we calculated the annual harmonic of the 21 years of altimetry data at each grid point of the domain. In this paper, we work with the detrended SST, NHF and SLA data, and we only analyze the linear trend of the SLA.

3.3. Ekman Transport

To analyze the wind effect on the SLA variability we calculate the cross-shore Ekman transport along the coast as:

$$M = \frac{\tau}{\rho_0 f}\hat{t} \qquad (8)$$

where τ is along-shore wind stress described in section 2.4, ρ_0 is the seawater density and f the Coriolis parameter. First, we eliminate the outliers that exceed the range of values accepted by QuikSCAT, that is $\pm$2.5 Pa. Then we averaged all the January values for the entire record, and so on for the remaining months. We choose segments parallel to the coastline at different latitudes where we apply equation (8) to each segment centered in the middle point. The reference density used is $\rho_0 = 1024$ kg m^{-3} and the Coriolis parameter is calculated for each segment.

4. Results and Discussion

4.1. Linear Trend

The linear trend of SLA in the SWACS for the period January 1993 to December 2013 is positive throughout the domain, ranging between 1 and 5 mm/yr (Figure 2). The sea level trend and its spatial distribution is not sensitive to whether the seasonal cycle is removed or not. Here we show the trends of the SLA with the seasonal cycle. All the trends larger than 0 mm/yr are statistically significant at the 95% confidence level (CL). There are three regions in the study area with large positive SLA trends ($>$ 4 mm/yr): i) in the outer shelf north of 38°S, ii) in San Matías Gulf at 42°S and iii) in a coastal region at 50°S. At San Jorge Gulf (see Figure 1 for location) a relative minimum ($<$ 2 mm/yr) is observed (Figure 2).

Most of the SWACS is dominated by trends of 2–3 mm/yr (mean value: 2.5 mm/yr) that are close to the global average trend of 3.2 mm/yr reported by *Meyssignac and Cazenave* [2012] using satellite altimetry data for the last two decades. The studies of sea level rise at global and regional scales have demonstrated that the steric effect associated with global warming is one of the main contributors [*Cazenave and Llovel*, 2010; *Meyssignac and Cazenave*, 2012].

One of the three areas with largest positive trends is observed in the outer continental shelf, between 36 and 38°S, corresponding to the region under the influence of the Brazil and Malvinas currents [e.g., *Saraceno*

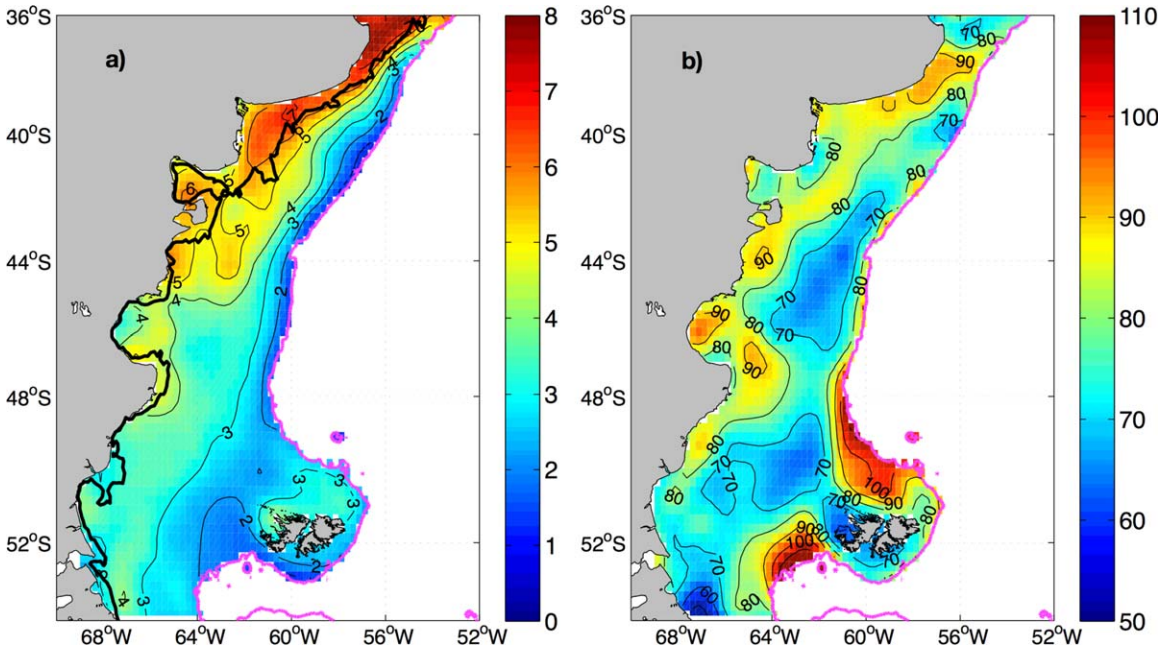

Figure 3. (a) Annual amplitude (cm) and (b) annual phase (days) distributions of SLA derived from 21 years of satellite altimetry (1993–2013). The phase indicates the number of days after 1 January when the maximum sea level is observed. The magenta and black lines indicate the 200 m and 50 m isobaths respectively.

et al., 2004]. It has been shown that this region presents a positive trend in SST and sea level, which is associated with a southward migration of the position of the BC front [*Goni et al*., 2011; *Lumpkin and Garzoli*, 2011; *Sato and Polito*, 2008]. This migration is presumably caused by the southward migration of the semipermanent South Atlantic high-pressure system [*Barros et al*., 2008]. Such a migration might, locally, intensify the BC, which might, in turn, increase the SLA. *Goni et al*. [2011, Figure 10] showed the SSH linear trend offshore of the 200m isobath: the latitude range in which they observe maximum positive trends matches ours (36–38°S).

The near coastal region at 50°S has trends higher than 4 mm/yr close to the mouth of the Santa Cruz River (Figure 2). Thus, the observed trend could be a response to increased river discharge. However, a recent study by *Pasquini and Depetris* [2011] did not find significant trends in the Santa Cruz river discharge. We also explored if changes in wind stress could explain the observed trends in the SLA in the region through upwelling or downwelling process. NCEP wind stress data were analyzed here instead of QuikSCAT data since the former coincides with the altimetry time period while the latter does not. No significant trend in the wind stress that could explain the above-mentioned process near Santa Cruz River mouth was found.

On the other hand, using NCEP data, we do find a positive trend for the wind stress component parallel to the coast in the San Matías Gulf (significant at the 95%CL, not shown) where SLA shows large ($>$ 4 mm/yr) positive trends (Figure 2). A positive trend in the meridional wind stress component (which is the component parallel to the coast in the San Matías Gulf) will imply onshore flow in the Ekman layer and therefore a positive trend in near coastal SLA.

Further studies are needed to more precisely determine the physical mechanisms that cause the large rates of increasing sea level at the coastal locations near 50°S and 42°S. Given their near-coastal locations, it is also possible that these regions are affected by errors in the altimeter data retrievals due to the proximity of land or to a bad interpolation of the along-track data. To test the latter hypothesis, we estimated the SLA trend in the two coastal areas from the along-track data (T/P, Jason-1, Jason-2, ENVISAT) provided by the Center for Topographic studies of the Ocean and Hydrosphere (CTOH). The resulting linear trends in both regions are larger than 4 mm/yr, in very good agreement with the trend obtained from the gridded data.

Sea level trend estimates from tide gauges are also reported by National Oceanic and Atmospheric Administration (NOAA) (tidesandcurrents.noaa.gov/sltrends/sltrends.html) at other locations along the Argentine

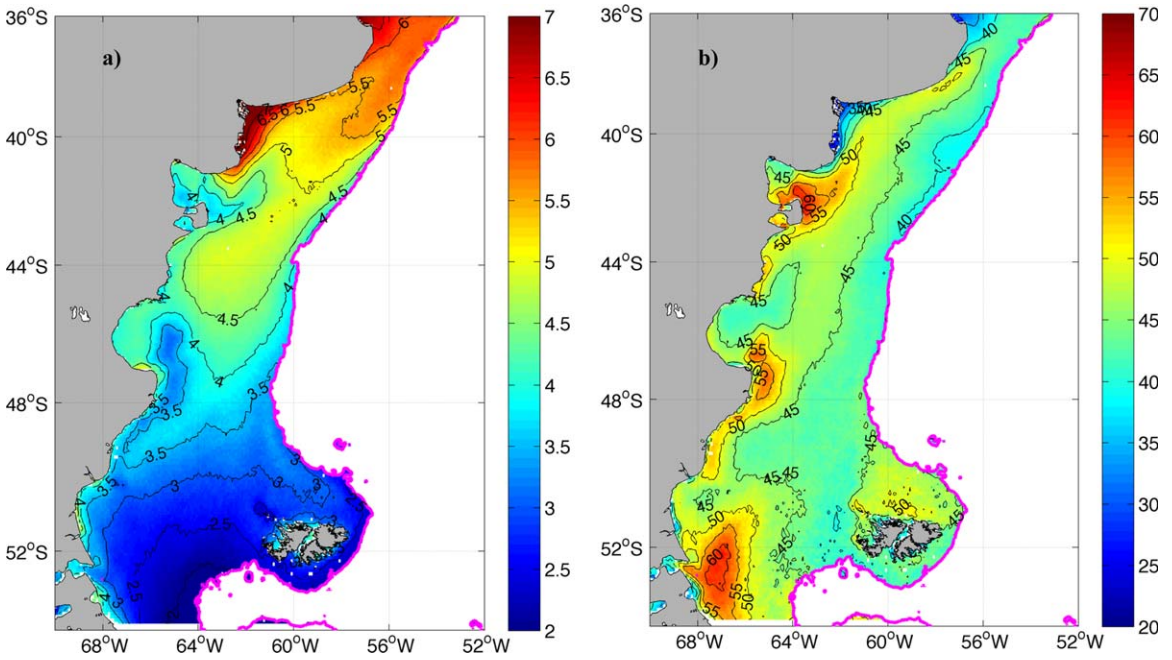

Figure 4. (a) Annual amplitude (°C) and (b) annual phase (days) distributions of SST derived from 11 years of MODIS SST data (2003–2013). The phase indicates the number of days after 1 January when the maximum SST is observed. The magenta line indicates the 200 m isobath.

coast. However, our results are not directly comparable with those reported by NOAA because a careful inspection of the original sea level data shows that the time series (i) are not coincident in time with the altimetry record and (ii) present significant gaps. Nevertheless, we did estimate the sea level trend from the tide gauge located in Mar del Plata, provided by Permanent Service for Mean Sea Level (PSMSL, http://www.psmsl.org/) for the period January 1993 to December 2013. This time series shows a linear trend of 2.92 mm/yr (95% CL) which is in good agreement with our estimate of 2.87 mm/yr (Figure 2).

4.2. Annual Signal

Figure 3 shows the annual amplitude and phase of SLA. Amplitudes larger than 5.5 cm are located in a coastal band north of 44°S, reaching the maximum (7–8 cm) between 38 and 36°S (Figure 3a). The offshore edge of this high-amplitude region closely follows the 50 meter isobath. Values lower than 4 cm are mostly located close to the shelf break and south of 44°S. The distribution of the SLA annual amplitude shares some similar features with the annual amplitude of the SST (Figure 4a): large amplitudes (5–7°C) are dominant north of 44°S and small amplitudes (2–4°C) are located south of 44°S. The annual amplitude of the SST shows a narrow low-amplitude band near the shelf break as in the SLA annual amplitude. However, the SLA narrow band extends farther north along the shelf break and the SST amplitude pattern has a midshelf maximum between 40 and 49°S that is not found in the SLA pattern.

The annual phase pattern of the SLA (Figure 3b) is dominated by a 60–90 day phase. This means that the annual cycle of SLA peaks between early and late March. We also observe relative SLA phase maxima (days 100–110, 10–20 April) northeast and southwest of the Malvinas Islands. On the other hand, the annual phase of SST is dominated by a 40–50 day phase, indicating that SST maxima occur approximately a month earlier than SLA maxima. There is less similarity between the two spatial patterns of annual phase than found in the annual amplitudes. In the middle shelf between 51 and 41°S, north of 37°S and closer to the coast (39°S–41°S), low values of the annual phase are observed (Figures 3b and 4b). In the southern part of the shelf, in particular close to the coast and close to the Malvinas Island, the SST annual phase distribution shows some differences compared with the SLA annual phase (Figures 3b and 4b). Maximum values of annual phase of SST are located near the coast at 42°S, 47°S and 53°S (Figure 4b). These regions approximately coincide with those observed in SLA, except for the southern location (Figure 3b). The spatial distribution of the annual amplitude and phase of SLA do not have significant differences when the calculation

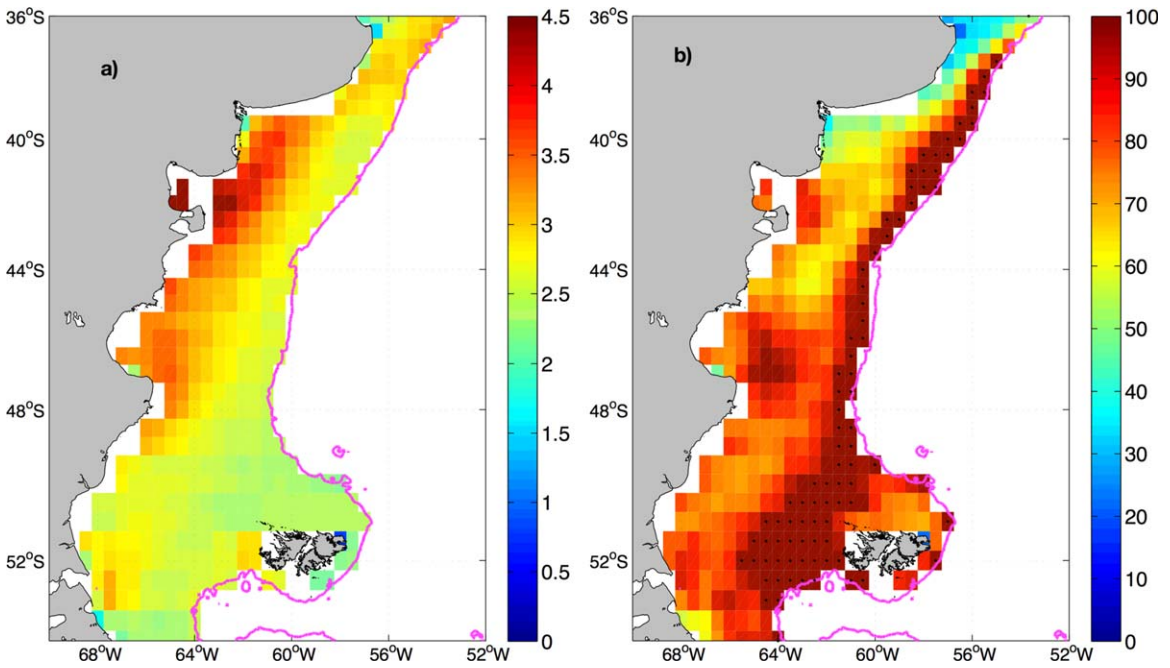

Figure 5. (a) Annual amplitude (cm) of SLA derived from equation (5) and using the NCEP CFSR net heat flux. (b) Ratio (%) between the annual amplitude of the steric height anomaly (SLA_{NHF}) and the SLA for each pixel. The black dots indicate ratios larger than 100%. The magenta line indicates the 200 m isobath.

is carried out using only AVISO-SLA data for the time period concomitant with the MODIS SST time period (2003–2013). Thus, our analysis is based on AVISO-SLA data for the 1993–2013 time period.

Temperature changes in the water column are primarily associated with the annual cycle of NHF (equation (5)). The response to NHF changes includes the SST, which is an indirect indicator of seasonal changes in the heat content of the water column. When the NHF is positive (negative), the ocean gains (losses) heat and the surface starts to warm (cool). As the water column heats (cools), it expands (contracts), leading to the observed increase (decrease) in SLA. The time required to warm (cool) the water column depends on the stratification and the depth of the bottom or mixed layer. In the southern region (40°S–55°S), *Rivas* [2010] observed that the SST maximum occurs later (earlier) and the SST amplitude decreases (increases) when the stratification is weaker (stronger). This explains why the amplitude of SST decreases and the phase increases near shore, where the water column is nearly homogeneous due to the enhanced mixing induced by the interaction of strong tidal currents with the bottom. In the northern coastal region, 36–41°S, the temperature is controlled by sea-air heat exchange and bathymetry [*Lucas et al.*, 2005]. Well-mixed waters dominate this region inshore of the 40–60 m isobaths [*Lucas et al.*, 2005]. This relatively shallow and well-mixed region is where the maximum annual amplitudes in SLA and SST are observed. A combination of shallow depth and high temperature generates a higher thermal steric height. Next we explore the relationship between surface fluxes and SLA.

4.2.1. Thermosteric Height

The purpose of this section is to analyze whether the heating and cooling of the water column through net surface heat fluxes explain the changes in annual SLA. Thus, we calculate the thermosteric height anomaly (η'_s) with equation (5) using two NHF data sets, NCEP CFSR and OAflux (section 2.2). In Appendix A we analyze the sensitivity of the estimate of η'_s to the relatively low spatial resolution of OAflux NHF (1°x1°) compared with NCEP CFSR (0.5°x0.5°). This analysis indicates that there are no significant impacts associated with the spatial resolution of NHF. In this section we present the results using NCEP CFSR NHF. Figure 5a shows that the annual amplitude of the η'_s ranges from 2 cm to 4.5 cm. In the northern region, these amplitudes are significantly lower than the annual amplitudes of SLA in Figure 3a. Regions of relatively high η'_s amplitude (3.5–4.5 cm) are observed between 39°S and 48°S along the inner half of the shelf. Amplitudes along the shelf-break and south of 48°S are lower than 3 cm. If the NHF is the main forcing of the SLA, the annual component of the η'_s (hereafter SLA_{NHF}) would explain most of the variance of the annual component of SLA. The ratio SLA_{NHF}/SLA is shown in Figure 5b. This ratio is calculated as the amplitude of SLA_{NHF}

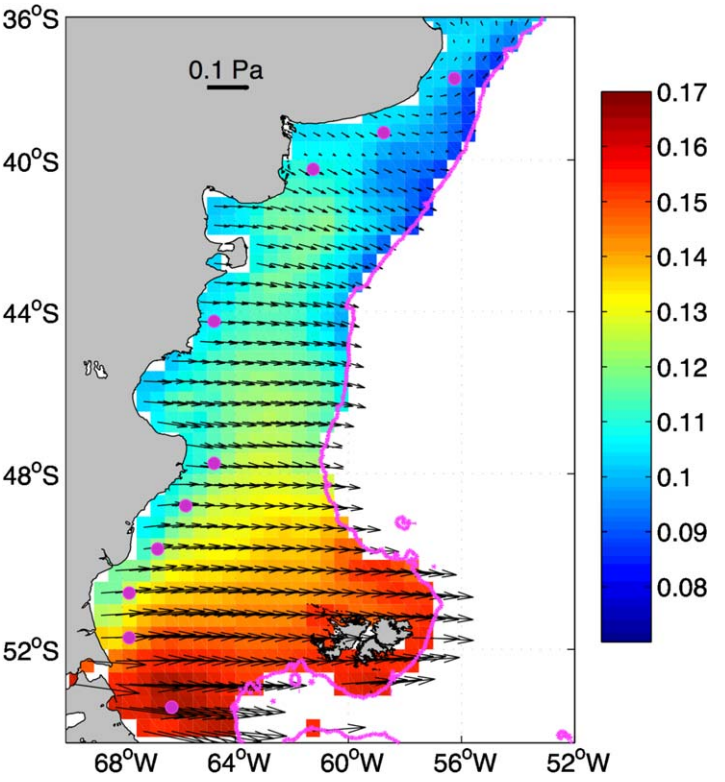

Figure 6. 9 year (2000–2008) mean wind stress magnitude (Pa) and wind stress vectors derived from QuikSCAT satellite data. The magenta dots show the grid points where the time series of the along shore wind stress were extracted to compute the cross-shore Ekman transports. The magenta line indicates the 200 m isobath.

divided by the amplitude of SLA interpolated to the NHF grid. The amplitude of the thermosteric height anomaly explains up to a 100% of the annual SLA variation, in particular in the southern portion of the SWACS (Figure 5b). At larger spatial scales similar results were obtained in the Atlantic and Pacific Ocean at mid and high latitudes [*Stammer*, 1997] and in the North Atlantic [*Ivchenko et al*., 2007]. A similar analysis shows also a good agreement between the steric-effect and seasonal SLA in coastal areas such as northeast of New Zealand [*Bell and Goring*, 1998], the Caribbean Sea [*Alvera-Azcárate et al*., 2008] and the Gulf of Cadiz [*Laiz et al*., 2013]. Near the Malvinas Island, over the shelf break and between 46.5°S and 47.5°S (centered at 64.5°W), estimated SLA_{NHF} amplitudes are larger than SLA amplitudes (ratios larger than 100%) (Figure 5b). A possible cause for this observation is the nonseasonal exchange between shelf and open ocean waters. For instance, export of relatively warm, low-density shelf waters and inflow of colder and denser MC waters would lead to lower SLA, an effect not associated with the net heat flux through the sea surface. A flux of MC waters to the shelf would imply an advective heat loss in the outer shelf and therefore lower SLA than implied by the NHF. This hypothesis cannot be corroborated using available in situ data. Recent modeling studies and satellite observations suggest that such mass exchanges across the shelf break may be significant at some locations [*Matano et al*., 2010]. Similarly, recurrent intrusions of slope waters have been observed near 41°S [*Piola et al*., 2010]. This process may explain the reduced annual SLA amplitude observed at that location (note the onshore deflection of the 3 cm contour in Figure 4a). In addition, there is modeling and observational evidence of upwelling along the shelf break south of ~38°S [*Combes and Matano*, 2014; *Matano et al*., 2010; *Valla and Piola*, 2015], which would significantly alter the heat balance in this region [*Valla and Piola*, 2015].

In contrast, in the mid shelf north of 42°S the percentage of annual amplitude of SLA explained by the net surface heat flux is lower than 60% (Figure 5b). The fact that the thermosteric height explains a minor percentage of the SLA annual amplitude north of ~45°S suggests that other mechanisms significantly contribute to the annual cycle of SLA. In the following sections we investigate two possible mechanisms that may contribute to the annual SLA: (i) wind stress variability (section 4.2.2) and (ii) the halosteric SLA (section 4.2.3). In addition, we study the accuracy of the WOA data used to compute the thermal expansion coefficient in the SWACS (see Appendix B). Results of this analysis show that using observations instead of WOA data to compute the thermal expansion coefficient improves the amplitude of SLA_{NHF} estimation but does not fully explain the annual SLA variability.

4.2.2. Wind Effect

Wind variability in the northern SWACS region is dominated by a relatively large seasonal component [*Palma et al*., 2004b], whereas south of 40°S the wind stress regime is characterized by intense westerlies and lower seasonal variations. Figure 6 shows the annual mean wind stress in the region. These data reveal

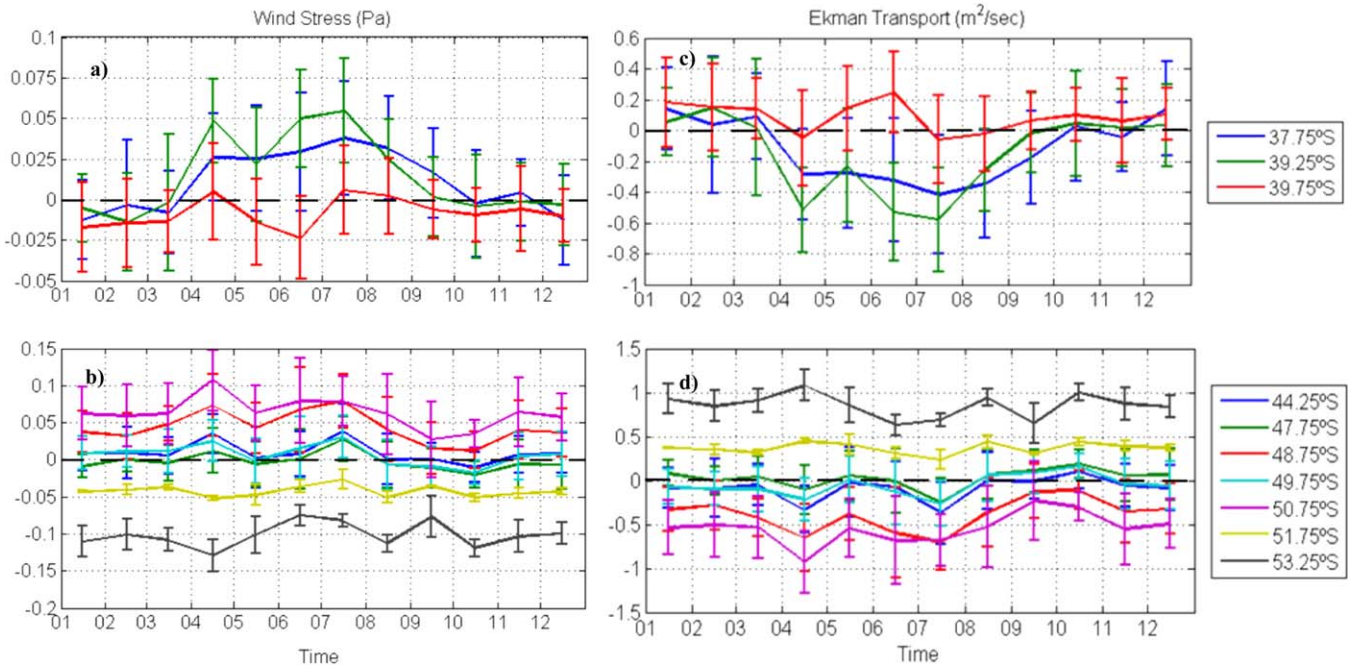

Figure 7. The annual cycle of: (a, b) the along-shore component of the wind stress (Pa) and (c, d) the corresponding cross-shore Ekman transport (m^2/s) at different locations along the coast. The top (bottom) plots correspond to points in the northern (southern) shelf regions (see Figure 6 for locations).

the significant intensification of the westerlies south of 40°S. In contrast, north of 40°S, the wind stress does not present a dominant direction, and the intensity is lower.

To analyze whether the seasonal variability of the along-shore wind may affect the seasonal signal of SLA, we calculate the cross-shore Ekman transport at several points along the coast (Figure 6) using equation (8) (section 3.3). Similar Ekman transport estimates have been carried out in different parts of the world. For example, along the central coast of Chile (27°S and 40°S) the off-shore Ekman transport oscillates between ∼1.5 Sv in summer and ∼0.6 Sv in winter [*Aguirre et al*., 2012]. These magnitudes are larger than the transport estimated in the northern part of our study area (Figure 7), where positive (negative) transports correspond to upwelling (downwelling) and to a decrease (increase) in the sea level close to the coast. We observe that the Ekman transport at 37.75°S and 39.25°S (Figure 7c) present an annual variation with a weak offshore transport (∼0.1 m^2/s) during summer and spring, and an intense onshore transport (−0.4 to −0.6 m^2/s) during autumn and winter. These transports would induce downwelling and increased SLA during April–August (autumn-winter) and weak upwelling with mildly decreased SLA during October–March (spring-summer). However, the SLA peaks in March–early April, three months before the maximum onshore transport (July). South of 40°S, the time series of Ekman transport presents little seasonality (Figure 7d). These cross-shore transport estimates are in agreement with the results reported by *Lucas et al*. [2005].

Although at 37.75°S and 39.25°S the winds are downwelling favorable in autumn-winter, the Ekman transport generated is possibly not intense enough (Figures 7a–7c) to manifests itself in the SLA signal. This hypothesis is corroborated by computing empirical orthogonal functions (EOF) of the reconstructed (harmonic) annual SLA in a region close to the coast between 36°S and 39°S (Figure 8). The first mode explains more than 98% of the variance and shows the largest values south of 38.5°S (Figure 8a). The second mode explains only the 1.5% of the variance and has a complementary spatial pattern to the first mode (Figure 8b). The first mode maximizes in mid-March and minimizes in mid-September (blue line Figure 8c) and is therefore associated with the steric effect. The timing (phase) of the second mode (Figure 8d) is very similar to that of the Ekman transport calculated at 37.75°S (Figure 7c), precisely where the second mode spatial pattern maximizes (Figure 8b). Since the phase of the second mode may be determined by the EOF requirement to be independent of the first mode, placing its maximum 3 months after the first mode, we estimated the EOF of the monthly climatological values of SLA. The result (not shown) returns four principal modes of which the first two (first mode 96.44%, second mode 1.92%) coincide with the modes found in

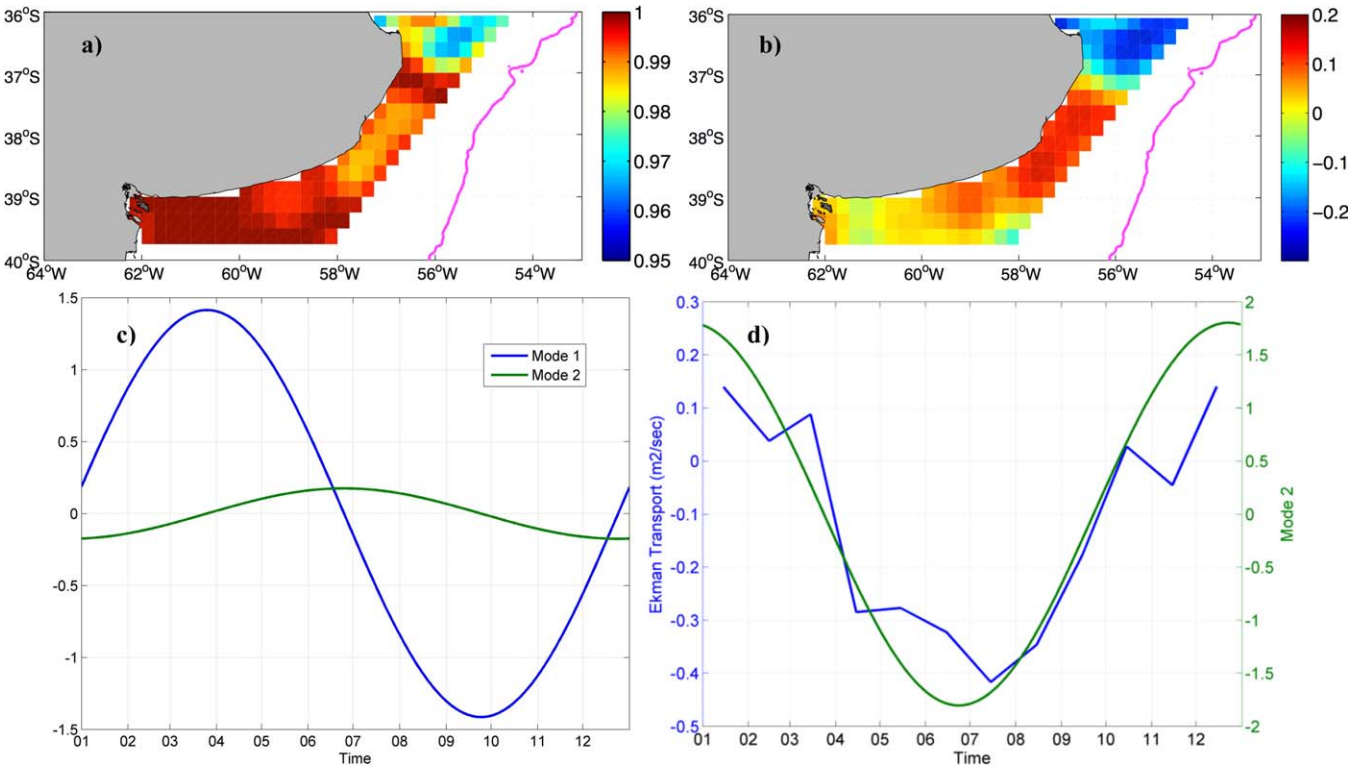

Figure 8. Leading EOF modes of annual variability of SLA. (top) Factor loading corresponding to (a) the first mode (98.5%) and (b) second mode (1.5%). The magenta line indicates the 200 m isobath. (bottom) (c) factor scores corresponding to the first mode (blue line) and second mode (green line). Both time series are normalized by the standard deviation of mode 1. (d) Time series of the cross shore Ekman transport (blue line) at 37.75°S (see Figure 6c) and Mode 2 multiplied by −1 to ease the comparison with Ekman transport.

the annual harmonic of SLA. Given the small fraction of variance explained by the second mode, the EOF analysis can only be used to reinforce the result that the steric effect is the main process responsible of the annual SLA variability between 36.5 and 38°S, despite the fact that it is not directly associated with changes in net heat flux. In contrast, as discussed in the introduction, the wind variability plays a dominant role in the SLA variability in the RdP estuary and north of the RdP [*Saraceno et al*., 2014; *Strub et al*., 2015].

The southern part of the shelf is characterized by strong westerly winds: the 9 years mean wind stress in this region varies between 0.1 and 0.17 Pa (Figure 6). However, our results show that in two latitudes (Figure 7b, 53.25°S and 50.75°S) the along-shore wind stress component is sufficiently strong to cause a significant cross-shore transport, similar to those estimated off Chile. These intense transports do not show a seasonal variation and the variability is low relative to the mean values. Therefore, we suggest that the Ekman transport does not have a significant effect on the annual signal of SLA in the southern portion of the continental shelf.

4.2.3. Halosteric Height

In this section, we discuss the halosteric component in the northern part of the region. The main freshwater supply in the SWACS comes from the RdP. The RdP river mouth is located at approximately 35°S and its mean discharge is of 23,000 m^3/s [*Borús et al*., 2013]. There is evidence that the RdP plume reaches latitudes as far south as 37–38°S during austral summer [*Piola et al*., 2008a, 2008b; *Möller et al*., 2008]. Thus, our hypothesis is that incoming fresh water from the RdP affects the steric height, making it necessary to include the thermal and the haline components. Figure 9 presents the annual amplitude of the halosteric height derived from WOA09, computed using the second term on the right-hand side of equation (4). As expected, the haline height is higher north of 38°S, increasing toward the RdP (Figure 9). Between 36°S and 39°S the shelf is quite narrow and the 1° spatial resolution of the WOA09 may not adequately represent the spatial variation of salinity and temperature near the coast. Moreover, the WOA09 database overestimates the values of both salinity and temperature at depth, and presents values at 50 m depth in regions where the bottom is shallower than 50 m. Under these circumstances we can give an approximate estimate of the

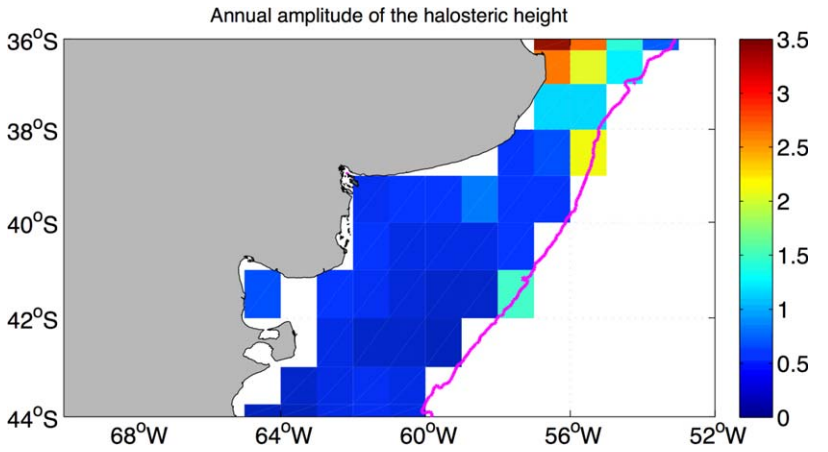

Figure 9. Annual amplitude (cm) of the halosteric height estimated with WOA09 data. The magenta line indicates the 200 m isobath.

areas where the haline component would be significant in the steric height, but we cannot precisely quantify its contribution to the SLA amplitude.

In section 4.2.2, we concluded that the wind does not contribute significantly to the annual cycle of SLA. However, the wind is the responsible force driving the RdP plume to the south-southwest during summer [e.g., *Piola et al*., 2008a]. Thus, we suggest that there are two relevant processes influencing the SLA annual cycle near the coast. First, the along-shore wind drives warm, low salinity waters from the RdP within a narrow (∼25 km) southward flowing coastal current [see *Möller et al*., 2008, Figure 9b]. This influence may extend beyond 38°S as suggested by *Lucas et al*. [2005]. Second, the southward extension of this warm low salinity water causes a sharp near-coastal SLA increase in summer, while in winter the seasonal cooling and the northward retreat of the low salinity plume lead to a sharp SLA drop. Thus, the coastal band south of the mouth of the RdP is a region of large seasonal SLA amplitude (Figure 3a) only partly associated with local heating effects (Figure 5b). Therefore, the annual scale of the satellite SLA might be capturing the sea level increase due to the incoming water but may be missing the narrow region of the southward flow.

To support our hypothesis that the annual amplitude of SLA is due to both components (haline and thermal) of the steric effect, we estimate the steric height difference between summer and winter using equation (3). We choose a vertical density profile from summer (February) and from winter (August) at 38°S where there are evidences of RdP waters. The steric height variation due to changes in the density is approximately 8 cm, which is much closer to the annual amplitude of SLA at that latitude (∼6.7 cm, Figure 3a) than to the annual amplitude of SLA_{NHF} (∼3 cm, Figure 5a).

4.3. Geostrophic Velocities

The sea level variation associated with the annual cycle of SLA discussed in the preceding sections generates changes in the geostrophic currents. Following the dynamical balances of realistic SWACS models [e.g., *Palma et al*., 2008] we can consider the geostrophic approximation valid to first order. In this section, we estimated the geostrophic velocities derived from the Absolute Dynamic Topography (ADT) estimated as annual SLA plus MDT. The purpose of considering the absolute geostrophic velocities is to analyze the relative importance of the annual changes in geostrophic velocity, derived from annual changes in SLA. For example, the annual geostrophic velocity anomalies change their direction from summer (equatorward) to winter (poleward) along the middle and outer shelf (not shown). However, it is relevant to ask if these current variations are strong enough to reverse the north-eastward mean circulation. Figures 10a–10l show the annual cycle of absolute geostrophic velocities for each month of the year superimposed on the mean monthly ADT fields. The general circulation of the SWACS is northeastward, with intense currents along the middle and outer shelf. In the inner shelf and within gulfs the mean currents are relatively weak and in some areas such as south of 48°S the mean flow is poleward. In El Rincón, San Matías Gulf and San Jorge Gulf (Figure 10a) there is a seasonal reversal of the coastal circulation. From January to April the currents are southward and from May to October are northward (Figures 10a–10l). In March (late austral summer), the

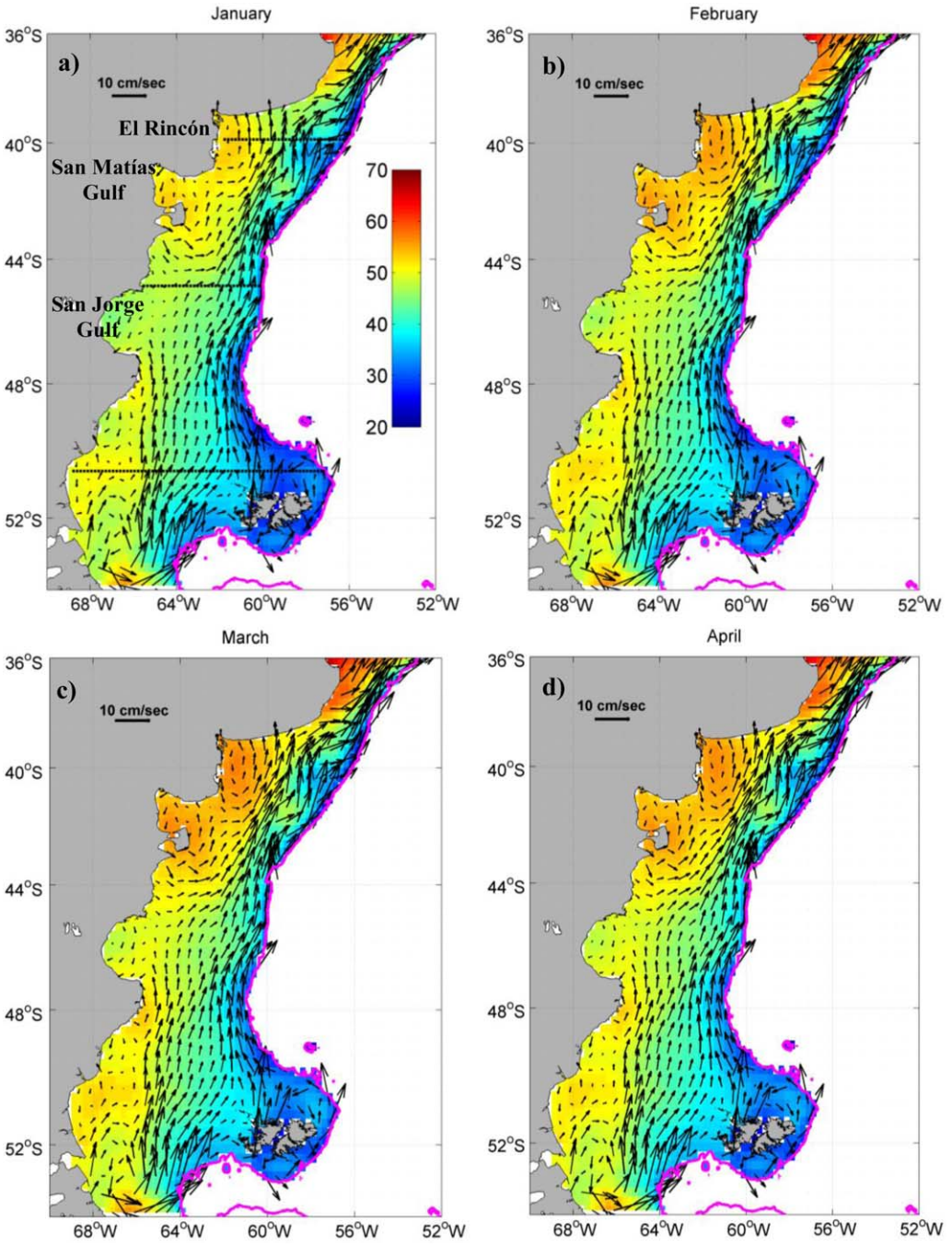

Figure 10. Maps of annual cycle of SLA+MDT (cm) and associated geostrophic velocities (vectors) for (a) January, (b) February, (c) March, (d) April, (e) May, (f) June, (g) July, (h)August, (i) September, (j) October, (k) November, and (l) December. (a–l) The magenta line indicates the 200 m isobath. The black dashed lines indicate the latitudes of Figure 11.

zonal gradient of the ADT is more evident than in winter, generating stronger geostrophic velocities. Figure 11 shows the direction and magnitude of the geostrophic velocities along three latitudes (39.87°S, 44.87°S and 50.63°S, see Figure 10a for locations) for late austral summer (March) and winter (September). March and September are chosen to display the summer and winter circulations because the SLA is maximum and minimum at these times. Figure 11 more clearly portrays the seasonal variability of the geostrophic currents, corroborating that though the spatial pattern changes from summer to winter, the north-northeast flow prevails throughout the year. Along 39.87°S and 44.87°S, the magnitude of the geostrophic velocity increases from 0–2.5 cm/s to approximately 20 cm/s toward the shelf break, with stronger flows in

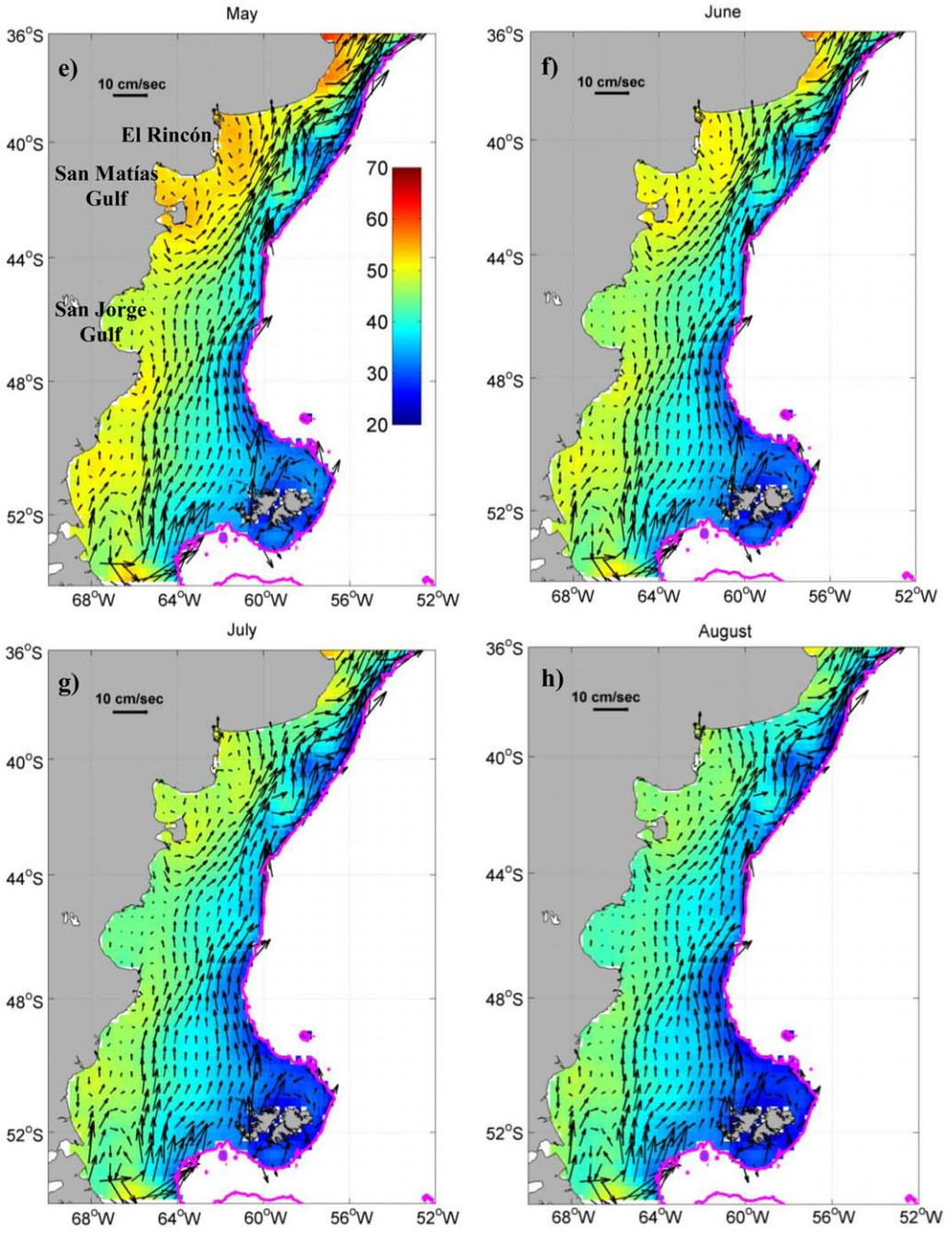

Figure 10. (continued)

March (Figure 11). At 39.87°S a seasonal change in the current direction close to the coast is observed. At 50.63°S the geostrophic velocity magnitude reaches up to 12 cm/s and its direction is mostly northward except near the shelf-break and close to the coast, where southward flow is observed. The somewhat smaller seasonal variations in the southern shelf indicate that the geostrophic velocity field in that region is mostly dominated by the MDT.

Strub et al. [2015] analyzed the geostrophic velocities derived from monthly mean ADT over the shelf from 27°S to 43°S. Their results in the region where their study overlaps with ours are in relatively good agreement. Both studies show equatorward currents with slight seasonality (see Figures 10 and 11, and their Figure 5 and supporting information). In El Rincón Bight, the model of *Palma et al.* [2008] presents an

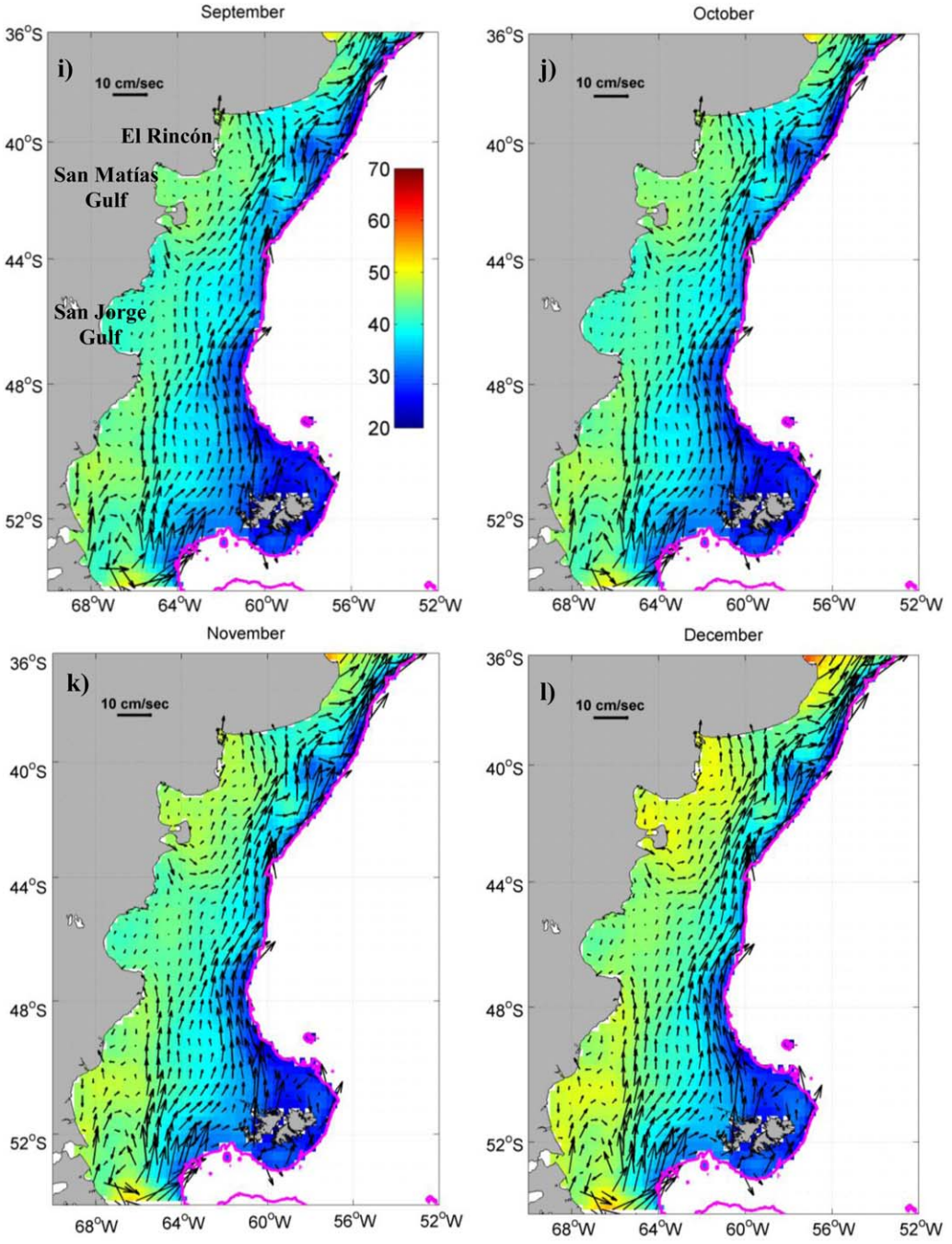

Figure 10. (continued)

anticyclonic flow that increases in July. *Strub et al*. [2015] confirm this flow pattern but argued that the altimeter cannot adequately represent the gyre due to its low spatial resolution. In contrast, our results indicate that the circulation in this region changes from summer to winter (Figure 11, 39.87°S). During the cold season there is no evidence of an anticyclonic gyre, while due to the reversal of the coastal flow in summer the gyre is almost fully developed (Figure 10c). The discrepancies in the spatial pattern derived by *Strub et al*. [2015] and our study might be due to the fact that to estimate the geostrophic velocities we only considered the contribution of the annual harmonic of SLA to the ADT.

South of 41°S, the seasonal circulation patterns modeled by *Palma et al*. [2008] present a strengthening of the northward current during autumn and a weakening during spring. This seasonal circulation pattern

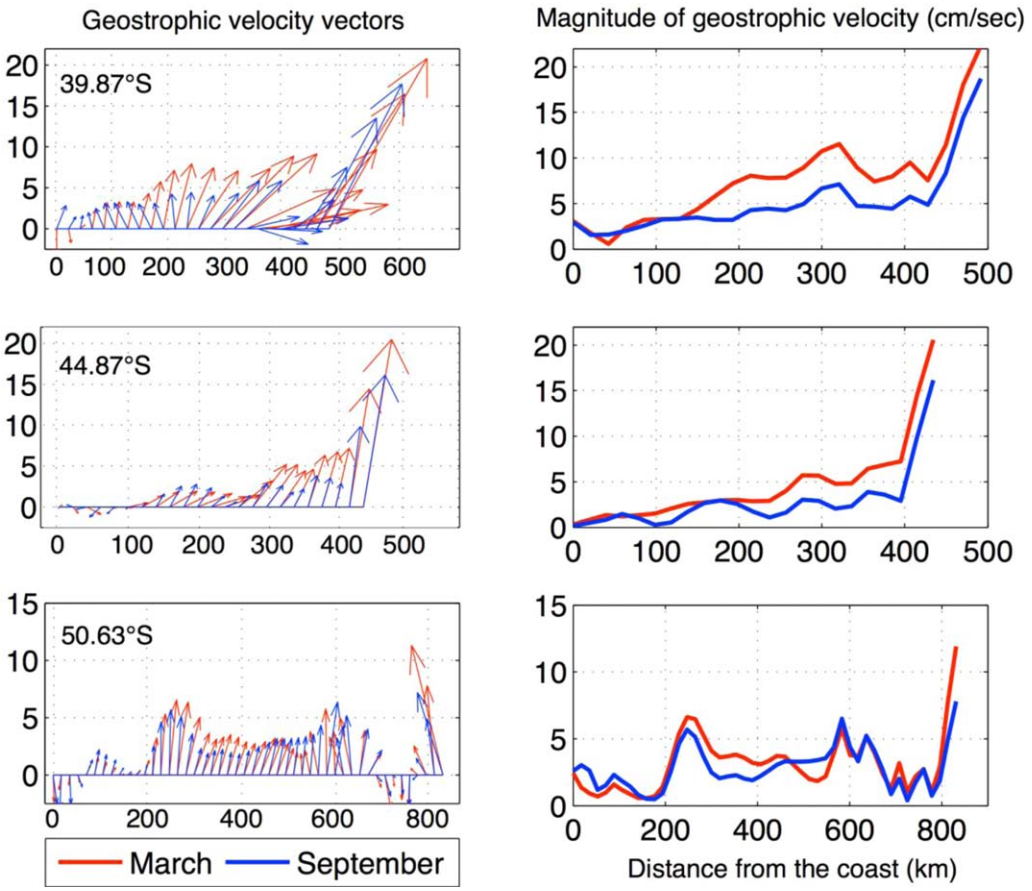

Figure 11. Mean geostrophic velocity vectors (left column) and magnitudes (right column) in cm/s derived from annual cycle of SLA+MDT for March and September along selected latitudes (see Figure 10a for locations).

does not match our altimeter derived circulation (Figure 10). The geostrophic velocities derived from the annual cycle of ADT diminish in late autumn and winter, and increase in late summer and early autumn. Thus, there is a small lag between the simulated circulation and the circulation derived from altimetry data using annual harmonic analysis. Our analysis indicates that at all latitudes the mean geostrophic velocity near the coast is small (∼2 cm/s) and increases offshore. This zonal variation of the meridional velocity is in relatively good agreement with the results of *Palma et al*. [2008].

5. Summary and Conclusions

We have analyzed the spatial structure of the annual harmonic and of the linear trend of sea level anomalies derived from satellite altimetry (SLA) in the SWACS region from 1993 to 2013. Combining the annual harmonic of SLA with the MDT we estimated the absolute dynamic topography to study the annual variability of the geostrophic velocities. Our results show that the linear trends of SLA range between 1 and 5 mm/yr. The regionally averaged linear trend is 2.5 mm/yr, similar to reported values of the global trend. The large trends observed near the shelf break north of 39°S are possibly associated with the southward drift of the BC in response to the southward displacement of the South Atlantic High Pressure system. The causes of the relative large values in two coastal areas, at 42°S and at 50°S, are discussed as a function of meridional wind stress and river discharge variations.

The annual amplitude of the detrended SLA is relatively large ($>$ 5.5 cm) over an extensive region north of ∼42°S and relatively low ($<$ 4 cm) farther south (Figure 3a). The lowest amplitudes of the annual SLA are observed along the continental shelf break. To investigate the processes leading to the annual signal of the SLA we computed the thermal component of the steric height (equation (3)) and compared the SLA with

the sea level anomaly estimated by assuming that it is entirely due to the net heat flux through the sea surface (SLA_{NHF}, Figure 5a). The thermosteric height variations explain up to 100% of the SLA annual amplitude south of 42°S. There are areas, such as near the Malvinas Island and along the shelf-break, where the ratio is higher than 100%. This means that the annual amplitude of the SLA_{NHF} overestimates the amplitude of SLA. We suggest that lateral advection and upwelling might locally alter the heat budget, leading to decreases in SLA amplitudes relative to that expected from the SLA_{NHF}.

North of 42°S the thermosteric height amplitude explains less than 60% of the SLA annual amplitude close to the coast (Figure 5b). To understand the origin of these differences we analyzed the effect of variations in the wind and in the halosteric sea level contributions. We also analyzed the spatial resolution of the NHF and the accuracy of the WOA data as a source of error in the estimation of the SLA_{NHF} (Appendices A and B). Results of our analysis of the wind effect showed that the cross-shore Ekman transport presents an annual signal only between 37.75°S and 39.25°S. However, the wind-driven onshore transport that favors sea level rise in coastal areas occurs in April–August, three months after the maximum annual SLA, suggesting that the annual variability in wind stress plays a minor role over the region.

Although the halosteric height is considered negligible compared to the thermosteric height over most of the ocean, it may play a significant role in determining the annual pattern of SLA in the northern SWACS. The spatial pattern of annual amplitudes of halosteric height estimated using WOA09 data shows higher values north of 38°S. This coincides with the region under the influence of fresh water derived from the Río de la Plata estuary. We suggest that the annual SLA is a combination of the thermosteric and halosteric effects in this region.

Finally, we estimated the geostrophic circulation of the SWACS as determined by the annual cycle of absolute dynamic topography (Figure 10). The general circulation pattern shows a north-northeast flow in the middle and outer shelf with a relatively small seasonality. The magnitude of the velocities increases toward the shelf-break, and it is greater in March (austral summer) than in September (austral winter). In the inner shelf there is a seasonal change in the direction of the currents that is not evident in the rest of the shelf.

This work allowed us to understand the sea level variability and geostrophic velocities in the SWACS at annual scale. This is a first step toward the study of sea level variability in the region at different temporal scales based on altimetry data.

Appendix A: NHF Spatial Resolution

In this section, we investigate whether the relative low spatial resolution (1x1 degrees) of the OAflux NHF database used to compute thermosteric height variations (equation (5)) might explain why SLA_{NHF} is lower in the northern region than in the southern region. The hypothesis is based on the fact that spatial scales in the northern region are smaller than in the south and thus spatial resolution could be important. To test this hypothesis we recomputed the SLA_{NHF} using the NCEP CFSR NHF (SLA_{CFSR}) database, which has a spatial resolution of 1/2 of degree. The 17 year (1993–2009) mean field of NHF from NCEP CFSR (NHF_{CFSR}) and OAflux (NHF_{OAflux}) are shown in Figure B1. Both data sets display similar magnitudes and spatial distributions, with relatively low positive heat flux near-shore (0–30 W/m^2), large positive heat flux around the shelf break (60 W/m^2) and negative heat fluxes farther offshore (lower than 50 W/m^2). As expected the NHF_{CFSR} reveals more details, particularly over the shelf and east of the Malvinas Current. Between 40°S and 36°S there is a marked zonal gradient in NHF_{CFSR} (Figure B1b), which is not well resolved by NHF_{OAflux} (Figure B1a). Near the Malvinas Island NHF_{CFSR} is ~40 W/m^2 (e.g., about 10 W/m^2 higher than NHF_{OAflux}). We also observe that the area dominated by negative values reach lower values in NHF_{CFSR} than in NHF_{OAflux}.

Figure B2a shows the amplitude of the annual SLA_{OAflux}. The spatial distribution of the annual amplitude is similar to the SLA_{NHF} amplitude (Figure 5a) but the maximum value decreases ~0.5 cm. Low amplitudes (~2.5 cm) are located along the shelf break, south of 48°S and between 37°S and 39°S. The near coastal region between 39°S and 44°S is dominated by large amplitudes (3.5–4 cm). The ratio between the amplitude of the SLA_{OAflux} and SLA (Figure B2b) indicates that the amplitude of the SLA_{OAflux} explains up to a 100% of the seasonal SLA variation in a portion of the domain. However, in relatively good agreement with the SLA_{NHF} analysis, north of 42°S the SLA percentage explained by SLA_{OAflux} is lower than 60% (Figure B2b). The area with low SLA_{OAflux}/SLA ratios is larger than the area observed in Figure 5b. Moreover, the

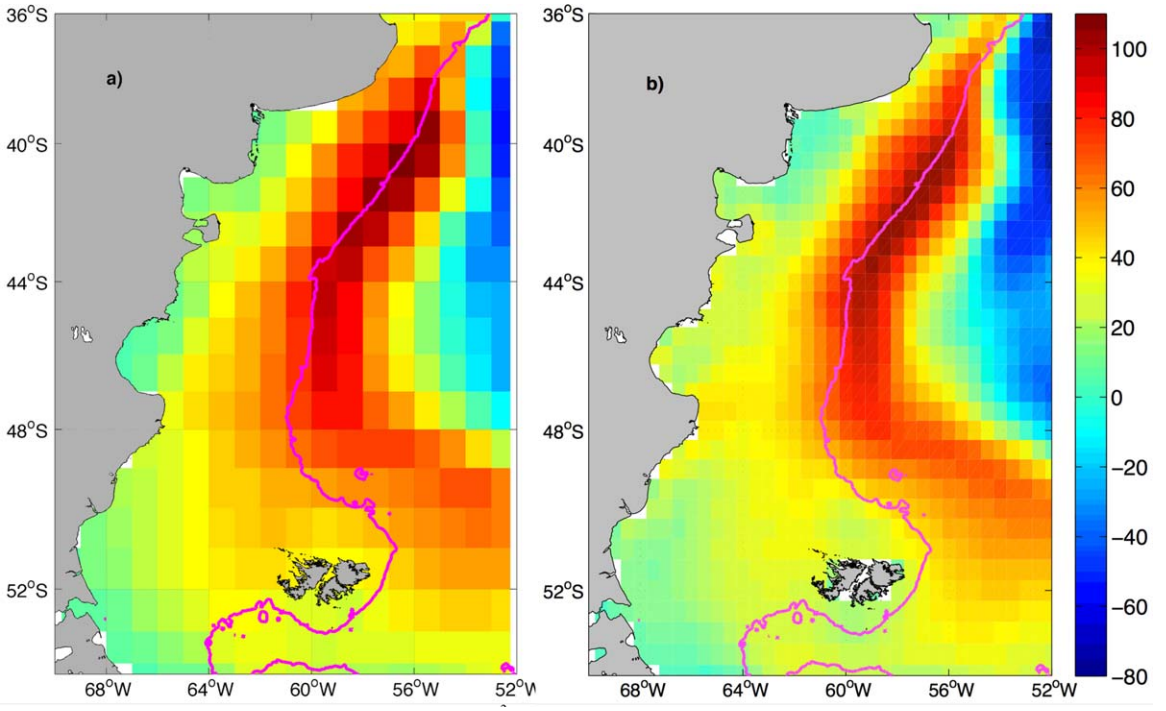

Figure A1. 17 year (1993–2009) mean field of Net Heat Flux (W/m^2) for: (a) Oaflux with a spatial resolution of 1° and (b) NCEP Climate Forecast System Reanalysis (CFSR) with a spatial resolution of 1/2°. Magenta line represents the 200 m isobath.

region displaying SLA_{OAflux}/SLA ratios larger than 100% occupy almost the same area observed in the SLA_{NHF} data (Figure5b). Thus, the discrepancy between SLA_{OAflux} and SLA cannot be explained simply by arguing that NHF_{OAflux} has a low spatial resolution.

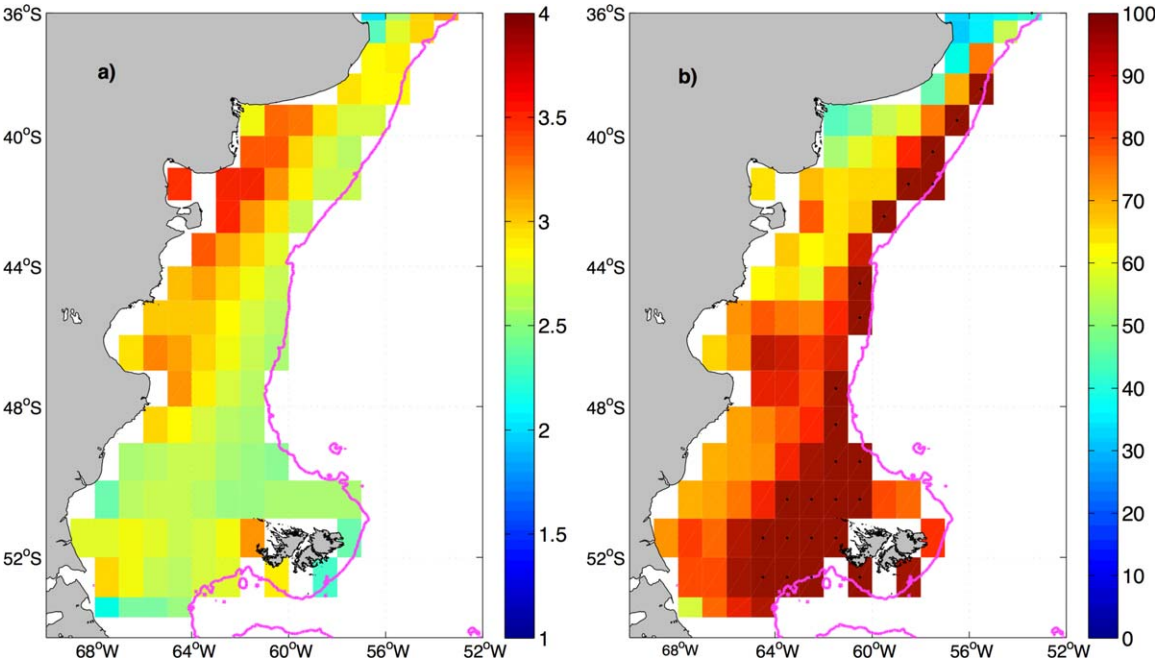

Figure A2. (a) Annual amplitude (cm) of SLA_{NHF} derived from equation (5) and using OAFLUX net heat flux. (b) Ratio (%) between the annual amplitude of the steric height anomaly (SLA_{NHF}) and the SLA for each pixel. The black dots indicate ratios larger than 100%. The magenta line indicates the 200 m isobath.

Appendix B: WOA Accuracy

A critical parameter to compute the SLA in equation (5) is the thermal expansion coefficient (α). This coefficient is a function of T, S and pressure (P). The variability of α is mainly due to changes in T, and less to changes in S and P. In this Appendix we compare vertical density profiles and the thermal expansion coefficients of seawater derived from T, S and P from the WOA09 database and derived from available in-situ hydrographic data in three locations along the SWACS. We used the GSW oceanographic toolbox (see section 2.3).

Our hypothesis is that the WOA09 climatology may present smooth temperature and salinity profiles that could lead to significant errors in the estimate of the thermal expansion coefficient. Figure A1 shows in-situ density profiles at three different locations in the SWACS together with the closest WOA09 vertical density profiles for summer (March) and winter (September). The seasonal pycnocline during summer is well developed while in winter the water column is nearly homogeneous. Significant differences between the in-situ and WOA09 data can be observed, particularly in summer, when density profiles derived from WOA09 do not show the well-defined mixed-layer that is observed in the hydrographic observations (Figure A1a). We also observe that in-situ hydrographic profiles have a sharper pycnocline compared with WOA09, particularly in the southernmost latitude (Figure A1a). In winter and summer, the WOA09 density profiles present higher densities than the hydrographic observations (Figure A1).

We estimated the thermal expansion coefficients with both data sets for each month of the year to evaluate the impact of the discrepancies between density profiles on the thermal expansion coefficients at the monthly scale. Here we focus the comparison in late austral summer (March) as an example. Figure A2b shows the distribution of the WOA09 thermal expansion coefficient superimposed with the in-situ coefficient (circles) for March. Note that the magnitude of both coefficients is similar, but there are differences south of 40°S on the outer shelf. The linear correlation coefficient between the thermal expansion coefficients computed from hydrographic data and the nearest WOA09 is 0.62, which is significantly different from zero at the 95% confidence level (hereinafter 95% CL) for March. The analysis of the twelve climatological months shows that there are only two months, July and August, where the above-mentioned correlation is not significant (not shown).

To better quantify the differences between the two data sets we compare the annual variability of thermal expansion coefficients over a selected region (38–39°S and 56–57°W, see Figure A2b) where at least one hydrographic station is available for each month. We then estimate the thermal steric height variations using the thermal expansion coefficient derived from in-situ observations ($SLA_{in\text{-}situ}$). The amplitude of $SLA_{in\text{-}situ}$ (~2.8 cm) is about 0.3 cm larger than the SLA_{CFSR} amplitude (~2.5 cm) but does not reach the SLA amplitude (~4 cm). These results suggest that WOA09 derived thermal expansion coefficient in this region tends to underestimate the annual cycle of thermosteric height. Using in-situ data somewhat improves the

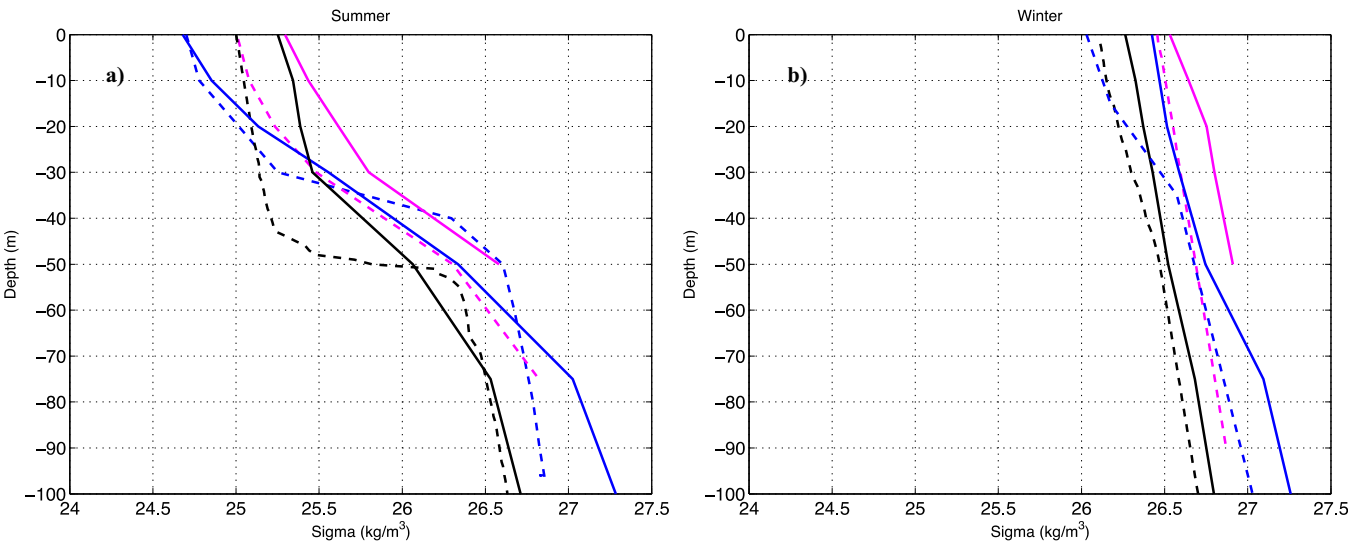

Figure B1. Vertical density (sigma-theta, kg/m^3) profiles for (a) summer (March) and (b) winter (September). The solid lines represent the WOA09 data and the dashed-dotted lines represent the in situ data. North (38.5°S–55.5°W), middle (43.5°S–60.5°W) and south (47.5°S–63.5°W) shelf are represented by blue, magenta and black lines, respectively.

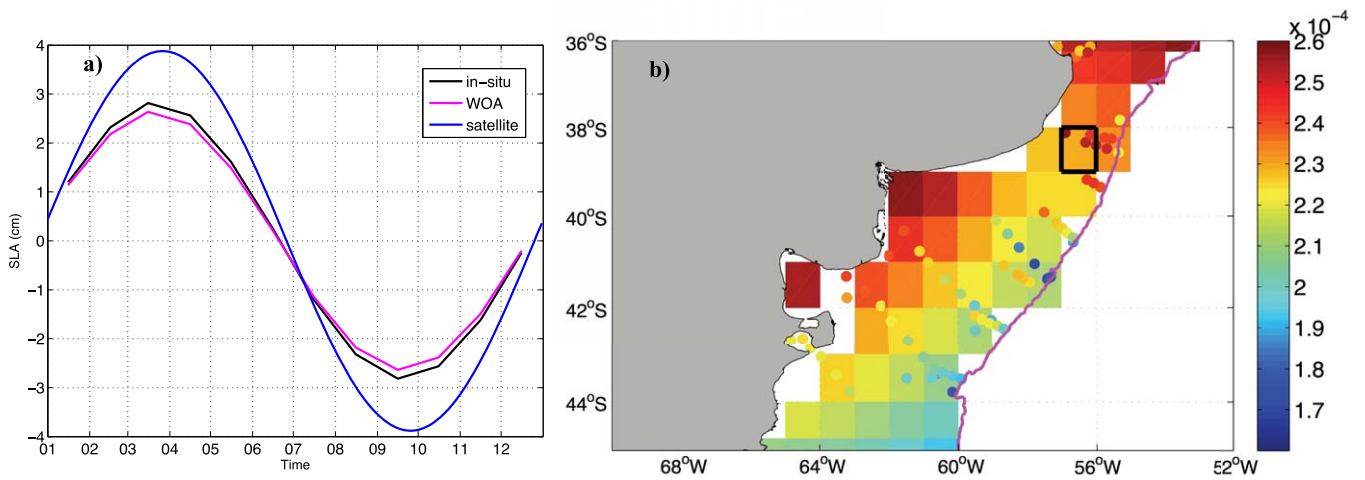

Figure B2. (a) Time series of the seasonal SLA (cm) derived from the altimeter (blue) and from the NHF using the thermal expansion coefficient calculated with WOA (magenta) and calculated with in situ data (black) collected within the region indicated in Figure B2b. (b) Distribution of thermal the expansion coefficient ($°C^{-1}$) derived from WOA for March superimpose with values estimated using in situ data (circles). The black rectangle delimits the region where the thermal expansion coefficient in-situ climatology shown in panel Figure B2a was extracted. The magenta line indicates the 200 m isobath.

computation but does not fully explain the amplitude of the annual signal SLA, further suggesting that advective processes are significant in the outer shelf.

Acknowledgments

This study is a contribution to EUMETSAT/CNES DSP/OT/12-2118, ANPCyT PICT 2012-0467, CONICET PIP 112-20110100176, PIO 133-20130100242, MinCyT/CONAE-001, MINCYT-ECOS-Sud A14U02 and UBACyT 20020100100840 Projects. ARP and LARE acknowledge the support of grant 3070 from the Inter-American Institute for Global Change Research (US National Science Foundation grant GEO-1128040). Support for PTS was provided by NASA grant NNX13AH22G. The altimeter products were produced by SSALTO/DUACS and distributed by AVISO with support from CNES. The along-track altimetry data used in this study were developed, validated, and distributed by the CTOH/LEGOS (http://ctoh.legos.obs-mip.fr), France.

References

Aguirre, C., O. Pizarro, P. T. Strub, R. Garreaud, and J. A. Barth (2012), Seasonal dynamics of the near-surface alongshore flow off central Chile, *J. Geophys. Res.*, *117*, C01006, doi:10.1029/2011JC007379.

Alvera-Azcárate, A., A. Barth, and R. H. Wiesberg (2008), The surface circulation of the Caribbean Sea and the Gulf of Mexico as inferred from satellite altimetry, *J. Phys. Oceanogr.*, *39*, 640–657.

AVISO (2014), *Ssalto/Ducas User Handbook: (M)SLA and (M)ADT Near-Real Time and Delayed Time Products SALP-MU-P-EA-21065-CLS*, 4.2 ed.

Barros, V. E., M. E. Doyle, and L. A. Camillioni (2008), Precipitation trends in southeastern South America: Relationship with ENSO phases and with low-level circulation, *Theor. Appl. Climatol.*, *93*, 19–33, doi:10.1007/s00704-007-0329.

Bell, R. G., and D. G. Goring (1998), Seasonal variability of the sea level and sea-surface temperature on the north-east coast of New Zealand, *Estuarine Coastal Shelf Sci.*, *46*(2), 307–318.

Bianchi, A. A., L. Bianucci, A. R. Piola, R. Pino, D., L. Schloss, A. Poisson, and C. F. Balestrini (2005), Vertical stratification and air-sea CO2 fluxes in the Patagonian shelf, *J. Geophys. Res.*, *110*, C07003, doi:10.1029/2004JC002488.

Borús, J., M. Uriburu Quirno, and D. Calvo (2013), *Evaluación de caudales diarios descargados por los grandes ríos del sistema del Plata al estuario del Río de La Plata*, Alerta hidrológico-Inst. Nac. del Agua y el Ambiente, Ezeiza, Argentina.

Boyer, T. P., J. I. Antonov, O. K. Baranova, H. E. Garcia, D. R. Johnson, R. A. Locarnini, A. V. Mishonov, D. Seidov, I. V. Smolyar, and M. M. Zweng (2009), World Ocean Database 2009, *Chapter 1: Introduction, NOAA Atlas NESDIS 66*, edited by S. Levitus, 216 pp., U.S. Govern. Print. Off., Washington, D. C.

Cazenave, A., and W. Llovel (2010), Contemporary sea level rise, *Annu. Rev. Mar. Sci.*, *2*, 145–173.

Combes, V., and R. P. Matano (2014), A two-way nested simulation of the oceanic circulation in the Southwestern Atlantic, *J. Geophys. Res.*, *119*, 731–756, doi:10.1002/2013JC009498.

Ducet, N., P. Y. Le Traon, and G. Reverdin (2000), Global high resolution mapping of ocean circulation from TOPEX/Poseidon and ERS-1 and -2, *J. Geophys. Res.*, *105*, 19,477–19,498.

Ferry, N., and G. Reverdin (2000), Seasonal sea surface height variability in the North Atlantic Ocean, *J. Geophys. Res.*, *105*, 6307–6326.

Gill, A. E., and P. P. Niiler (1973), The Theory of the seasonal variability of the ocean, *Deep Sea Res. Oceanogr. Abstr.*, *20*, 141–177.

Glorioso, P. D., and R. A. Flather (1997), The Patagonian Shelf tides, *Prog. Oceanogr.*, *40*, 263–283.

Gomez-Enri, J., A. Aboitiz, B. Tejedor, and P. Villares (2012), Seasonal and interannual variability in the Gulf of Cadiz: Validation of gridded altimeter products, *Estuarine Coastal Shelf Sci.*, *96*, 114–121, doi:10.1016/J.ECSS.2011.10.013.

Goni, G. J., F. Bringas, and P. N. DiNezio (2011), Observed low frequency variability of the Brazil Current front. *J. Geophys. Res.*, *116*, C10037, doi:10.1029/2011JC007198.

Ivchenko, V. O., S. Danilov, D. Sidorenko, Schröter, J., M. Wenzel, and D. L. Aleynik (2007), Comparing the steric height in the Northern Atlantic with satellite altimetry, *Ocean Sci.*, *3*, 485–490.

Ivchenko, V. O., S. Danilov, D. Sidorenko, J. Schröter, and M. Wenzel (2008), Steric height variability in the Northern Atlantic on seasonal and interannual scales, *J. Geophys. Res.*, *113*, C11007, doi:10.1029/2008JC004836.

Laiz, I., J. Gómez-Enri, B. Tejedor, A. Aboitiz, and P. Villares (2013), Seasonal sea level variations in the gulf of Cadiz continental shelf from in-situ measurements and satellite altimetry, *Cont. Shelf Res.*, *53*, 77–88.

Leuliette, E. W., and J. M. Wahr (1999), Coupled pattern analysis of the sea surface temperature and TOPEX/Poseidon sea surface height, *J. Geophys. Res.*, *29*, 599–611.

Levitus, S., et al. (2012), World ocean heat content and thermosteric sea level change (0-2000 m), 1955-2010, *Geophys. Res. Lett.*, *39*, L10603, doi:10.1029/2012GL51106.

Lombard, A., G. Garric, and T. Penduff (2009), Regional patterns of observed sea level change: Insights from a 1/4° global ocean/sea-ice hindcast, *Ocean Dyn.*, *59*, 433–449, doi:10.1007/s10236-008-0161-6.
Lucas, A. J., R. A. Guerrero, H. W. Mianzán, E. M. Acha, and C. A. Lasta (2005), Coastal oceanographic regimes of the Northern Argentine Continental Shelf (34-43°S), *Estuarine Coastal Shelf Sci.*, *65*, 405–420.
Lumpkin, R., and S. Garzoli (2011), Interannual to decadal changes in the western South Atlantic's surface circulation, *J. Geophys. Res.*, *116*, C01014, doi:10.1029/2010JC006285.
Matano R., E. D. Palma, and A. R. Piola (2010), The influence of the Brazil and Malvinas Currents on the Southwestern Atlantic Shelf circulation, *Ocean Sci.*, *6*, 983–995.
Matano, R. P., V. Combes, A. R. Piola, R. Guerrero, E. D. Palma, P. T. Strub, C. James, H. Fenco, Y. Chao, and M. Saraceno (2014), The salinity signature of the cross-shelf exchanges in the Southwestern Atlantic Ocean: Numerical simulations, *J. Geophys. Res. Oceans*, *119*, 7949–7968, doi:10.1002/2014JC010116.
McDougall, T. J., and P. M. Barker (2011), Getting started with TEOS-10 and the Gibbs Seawater (GSW) Oceanographic Toolbox, *SCOR/IAPSO WG127*, 28 pp. [Available at http://www.teos-10.org/pubs/Getting_Started.pdf.]
Meyssignac, B., and A. Cazenave (2012), Sea level: A review of present-day and recent- past changes and variability, *J. Geodyn.*, *58*, 96–109.
Möller, O. O., Jr., A. R. Piola, A. C. Freitas, and E. J. D. Campos (2008), The effects of river discharge and seasonal winds on the shelf off southeastern South America, *Cont. Shelf Res.*, *28*(13), 1607–1624.
Monterey, G., and S. Levitus (1997), Seasonal variability of the mixed layer depth for the world Ocean, *NOAA Atlas NESDIS 14*, 100 pp., Natl. Oceanic and Atmos. Admin., Silver Spring, Md.
Mork, K. A., and Ø. Skagseth (2005), Annual sea surface height variability in the Nordic Seas, in *The Nordic Seas: An Integrated Perspective*, edited by H. Drange et al., AGU, Washington, D. C., doi:10.1029/158GM05.
Palma, E. D., R. P. Matano, and A. R. Piola (2004a), A numerical study of the Southwestern Atlantic Shelf circulation: Barotropic response to tidal and wind forcing. *J. Geophys. Res.*, *109*, C08014, doi:10.1029/2004JC002315.
Palma, E. D., R. P. Matano, A. R. Piola, and L. Sitz (2004b), A comparison of the circulation patterns over the Southwestern Atlantic Shelf driven by different wind stress climatologies, *Geophys. Res. Lett.*, *31*, L24303, doi:10.1029/2004GL021068.
Palma, E. D., R. P. Matano, and A. R. Piola (2008), A numerical study of the Southwestern Atlantic Shelf circulation: Stratified ocean response to local and offshore forcing, *J. Geophys. Res.*, *113*, C11010, doi:10.1029/2007JC004720.
Pasquini, A. I., and P. J. Depetris (2011), Southern Patagonia's Perito Moreno Glacier, Lake Argentino, and Santa Cruz River hydrological system: An overview, *J. Hydrol.*, *405*(1), 48–56.
Passaro, M., P. Cipollini, and J. Benveniste (2015), Annual sea level variability of the coastal ocean: The Baltic Sea-North Sea transition zone, *J. Geophys. Res. Oceans*, *120*, 3061–3078, doi:10.1002/2014JC010510.
Piola, A. R., R. P. Matano, E. D. Palma, O. O. Möller, M. Charo, and E. J. D. Campos (2005), The influence of the Plata River discharge on the western South Atlantic shelf, *Geophys. Res. Lett.*, *32*, L01603, doi:10.1029/2004GL021638.
Piola, A. R., S. I. Romero, and U. Zajaczkovski (2008a), Space-time variability of the Plata plume inferred from ocean color, *Cont. Shelf Res.*, *28*, 1556–1567, doi:10.1016/j.csr.2007.02.013.
Piola, A. R., O. O. Möller Jr., R. A. Guerrero, and E. J. D. Campos (2008b), Variability of the subtropical shelf front off Eastern South America: Winter 2003 and summer 2004, *Cont. Shelf Res.*, *28*, 1639–1648, doi:10.1016/j.csr.2008.03.013.
Piola, A. R., N. Martinez-Avellaneda, R. A. Guerrero, Jadón, F. P., E. D. Palma, and S. I. Romero (2010), Malvinas-slope water intrusions on the northern Patagonia continental shelf, *Ocean Sci.*, *6*, 345–359.
Rivas, A. L. (2010), Spatial and temporal variability of satellite-derived sea surface temperature in the southwestern Atlantic Ocean, *Cont. Shelf Res.*, *30*, 752–760, doi:10.1016/j.crs.2010.01.009.
Ruiz Etcheverry, L. A., M. Saraceno, A. R. Piola, G. Valladeau, and O. O. Möller (2015), A comparison of the annual cycle of sea level in coastal areas from gridded satellite altimetry and tide gauges, *Cont. Shelf Res.*, *92*, 87–97.
Saraceno, M., C. Provost, A. R. Piola, J. Bava, and A. Gagliardini (2004), Brazil Malvinas Frontal System as seen from 9 years of advanced very high resolution radiometer data, *J. Geophys. Res.*, *109*, C05027, doi:10.1029/2003JC002127.
Saraceno, M., C. G. Simionato, and L. A. Ruiz Etcheverry (2014), Sea surface height trend and variability at seasonal and interannual time scales in the Southeastern South American continental shelf between27°S and 40°S, *Cont. Shelf Res.*, *91*, 82–94, doi:10.1016/j.csr.2014.09.002.
Sato, O. T., and P. S. Polito (2008), Influence of salinity on the interannual heat storage trends in the Atlantic estimated from altimeters and Pilot Research Moored Array in the Tropical Atlantic data, *J. Geophys. Res.*, *113*, C02008, doi:10.1029/2007JC004151.
Simionato, C. G., V. L. Meccia, R. A. Guerrero, W. C. Dragani, and M. N. Nuñez (2007), Río de la Plata estuary response to wind variability in synoptic to intraseasonal scales: 2 Currents' vertical structure and its implications for the salt wedge structure, *J. Geophys. Res.*, *112*, C07005. doi:10.1029/2006JC003815.
Smith, S. D. (1988), Coefficients for sea surface wind stress, heat flux and wind profiles as a function of wind speed and temperature. *J. Geophys. Res.*, *93*, 15,467–15,472.
Smith, W. H. F., and D. T. Sandwell (1997), Global sea floor topography from satellite altimetry and ship depth soundings *science, Science*, *277*, 1956–1962.
Song, Y. T., and T. Qu (2011), Multiple satellite missions confirming the theory of seasonal oceanic variability in the northern North Pacific, *Mar. Geod.*, *34*(3–4), 477–490.
Stammer, D. (1997), Steric and wind-induced changes in TOPEX/POSEIDON large-scale sea surface topography observations, *J. Geophys. Res.*: Oceans, *102*(C9), 20987–21009.
Strub, P. T., C. James, V. Combes, R. P. Matano, A. R. Piola, E. D. Palma, M. Saraceno, R. A. Guerrero, H. Fenco, and L. A. Ruiz- Etcheverry (2015), Altimeter-derived seasonal circulation on the southwest Atlantic shelf: 27°S–43°S, *J. Geophys. Res. Oceans*, *120*, 3391–3418, doi:10.1002/2015JC010769.
Tsimplis, M. N., and P. L. Woodworth (1994), The global distribution of the seasonal sea level cycle calculated from coastal tide gauge data, *J. Geophys. Res.*, *99*, 16,031–16,039.
Valla, D., and A. R. Piola (2015), Evidence of upwelling events at the northern Patagonian shelf break. *J. Geophys. Res. Oceans*, *120*, 7635–7656, doi:10.1002/2015JC011002.
Vinogradov, S. V., and R. M. Ponte (2010), Annual cycle in coastal sea-level from tide gauges and altimetry, *J. Geophys. Res. 115*, C04021, doi:10.1029/2009JC005767.
Volkov, D. L., and M. I. Pujol (2012), Quality assessment of a satellite altimetry data product in the Nordic, Barents, and Kara seas, *J. Geophys. Res.*, *117*, C03025, doi:10.1029/2011JC007557.
Yu, L., R. A. Weller, and B. Sun (2004), Improving latent and sensible heat flux estimates for the Atlantic Ocean (1988-1999) by a synthesis approach, *J. Clim.*, *17*, 373–393.